1   **Title**

2   Antiviral innate immune memory in alveolar macrophages following SARS-CoV-2 infection.

3

4   **Authors**

5   Alexander Lercher[1,*], Jin-Gyu Cheong[2,3], Chenyang Jiang[2,4], Hans-Heinrich Hoffmann[1], Alison W.

6   Ashbrook[1], Yue S. Yin[1], Corrine Quirk[1], Emma J. DeGrace[5], Luis Chiriboga[6,7], Brad R. Rosenberg[5],

7   Steven Z. Josefowicz[2,3], Charles M. Rice[1,*]

8

9   **Affiliations**

10   [1]Laboratory of Virology and Infectious Disease, The Rockefeller University, New York, NY 10065,

11   USA.

12

13   [2]Department of Pathology and Laboratory Medicine, Laboratory of Epigenetics and Immunity,

14   Weill Cornell Medicine, New York, NY, 10065, USA.

15

16   [3]Immunology and Microbial Pathogenesis Program, Weill Cornell Medicine, New York, NY, 10065,

17   USA.

18

19   [4]BCMB Allied Program, Weill Cornell Graduate School of Medical Sciences, New York, NY, 10065,

20   USA.

21

22   [5]Department of Microbiology, Icahn School of Medicine at Mount Sinai, New York, New York,

23   10029, USA.

24

25   [6]Department of Pathology, New York University Medical Center, New York, NY, 10016, USA.

26

27   [7]Center for Biospecimen Research and Development, New York, NY, 10016, USA.

28

29   *Correspondence: alercher@rockefeller.edu, ricec@rockefeller.edu

Abstract

Pathogen encounter results in long-lasting epigenetic imprinting that shapes diseases caused by heterologous pathogens. The breadth of this innate immune memory is of particular interest in the context of respiratory pathogens with increased pandemic potential and wide-ranging impact on global health. Here, we investigated epigenetic imprinting across cell lineages in a disease relevant murine model of SARS-CoV-2 recovery. Past SARS-CoV-2 infection resulted in increased chromatin accessibility of type I interferon (IFN-I) related transcription factors in airway-resident macrophages. Mechanistically, establishment of this innate immune memory required viral pattern recognition and canonical IFN-I signaling and augmented secondary antiviral responses. Past SARS-CoV-2 infection ameliorated disease caused by the heterologous respiratory pathogen influenza A virus. Insights into innate immune memory and how it affects subsequent infections with heterologous pathogens to influence disease pathology could facilitate the development of broadly effective therapeutic strategies.

Introduction

Immune memory is critical to fend off and ameliorate pathology of recurring diseases caused by pathogens. This is not only beneficial for the individual, but also forms the basis of herd immunity and population health [1]. Adaptive immune cells evolved to mount robust antigen-dependent responses and form long-lived memory cells. Complementary to this pathogen-specific immune memory, innate immune responses can facilitate the establishment of antigen-independent inflammatory memory [2]. This innate immune memory is defined as an epigenetic memory-state of a cell following encounter with inflammatory cues that alters subsequent immune responses [3,4]. The longevity of innate immune memory is influenced by cell type and stimulus and can be extended when established in immune progenitor cells in the bone marrow, tissue-resident stem cells or self-renewing tissue-resident macrophages [5–8]. The live-attenuated tuberculosis vaccine Bacillus Calmette-Guérin (BCG) elicits innate immune memory in humans that lasts for months and reduces child mortality caused by heterologous infectious agents [9–12]. Hence, innate immune memory is versatile and can provide long-lived cross-protection against heterologous pathogens.

2

59   Still, how this phenomenon influences real-word infectious encounters, such as serial infections

60   with heterologous pathogens, is poorly understood.

61   Respiratory pathogens have increased pandemic potential due to efficient airborne transmission

62   and often widespread illness within populations. The recent pandemic caused by severe acute

63   respiratory syndrome coronavirus 2 (SARS-CoV-2) and the resulting coronavirus disease 2019

64   (COVID-19) exemplified the far-reaching health and economic consequences of a new respiratory

65   pathogen [13] encountering a highly permissive, immune naïve host population. Development of

66   antigen-specific effective vaccines can help to achieve herd immunity requires time and success

67   is not guaranteed. Additionally, viruses can rapidly evolve to escape antigen-specific immune

68   memory [14]. Intervention strategies built upon the antigen-independent nature of innate immune

69   memory could provide increased robustness to achieve protective immunity in a naïve

70   population [4]. Alveolar macrophages are the most abundant immune cell type in the airway and

71   form a stem-like immune cell population that is the first line of defense against respiratory

72   pathogens [15–17]. Following bacterial or viral infections, alveolar macrophages are capable of

73   forming innate immune memory that can affect the outcome of secondary lung diseases, such as

74   bacterial pneumonia or cancer [8,18,19]. There is a gap in our understanding of innate immune

75   memory in the context of commonly circulating respiratory viruses. Specifically, how past

76   infections impact subsequent infections with unrelated viruses via epigenetic imprinting across

77   airway-resident immune cell lineages remains understudied. Such insights into the

78   establishment, maintenance, and recall of innate immune memory may therefore facilitate the

79   development of novel therapeutic strategies that target a broad range of respiratory pathogens.

80   In this study, we used a disease-relevant murine infection model of SARS-CoV-2 recovery to study

81   innate immune memory in airway-resident immune cells at single cell resolution and determine

82   how this influences infection outcome of secondary influenza A virus infection.

83

84

85

86

87

88 **Results**

89

90 Past SARS-CoV-2 infection leads to establishment of epigenetic imprinting in alveolar

91 macrophages.

92 We intranasally (i.n.) infected C57Bl/6J wild type mice with 6,000 PFU of the mouse-adapted

93 strain MA10 of SARS-CoV-2 (SARS2) [20]. Upon SARS2 infection, mice transiently lose body weight

94 loss, which they regain by 20-30 days post infection (dpi) (Figure 1A). SARS2 is cleared by 15 dpi

95 [20,21] and we confirmed absence of SARS2 RNA and antigen in lung tissue via RT-qPCR or histology

96 at 30 dpi (Figures S1A and S1B). Gene expression levels of many antiviral (*Ifit1*, *Bst2*, *Ifitm3*, *Isg15*)

97 and inflammatory genes (*Tnfa*, *Il6*) were not significantly different in bulk lung tissue of recovered

98 vs. naïve animals (Figure S1C). Immune cell profiling of bronchoalveolar lavage fluid (BALF) via

99 flow cytometry revealed no significant differences in numbers of alveolar macrophages

100 (CD45$^+$CD11c$^+$SiglecF$^+$), NK cells (CD45$^+$CD11c$^-$SiglecF$^-$NK1.1$^+$) or neutrophils (CD45$^+$CD11c$^-$

101 SiglecF$^-$CD11b$^+$Ly6G$^+$) in recovered vs. naïve mice (Figure S1D). The inflammatory milieu in

102 recovered and naïve airways was comparable. Among 32 detectable cytokines, only minor

103 differences were observed for IFN-γ, IL-2, IL-13 (decreased) and CXCL9, CCL19, CCL22, TIMP-1

104 (increased) in recovered vs. naïve BALF (Figures S1E and S1F). Flow cytometric analyses of major

105 subsets of bone marrow progenitor cells were comparable between recovered and naïve mice

106 (Figure S1G). CD4 and CD8 T cell numbers were significantly increased in recovered BALF and

107 expressed surface markers associated with effector memory (CD44$^+$CD62L$^-$) or tissue-resident

108 memory (CD69+CD103$^+$) cells (Figure S1H). Together, these data show that SARS2-recovered

109 animals do not retain active inflammatory responses or tissue pathology.

110 Next, we tested whether past SARS2 infection leads to sustained cell-intrinsic changes of airway-

111 resident cells. We investigated changes of chromatin accessibility and transcript levels of

112 individual cells in recovered (31 dpi) or naïve BALF (n = 3) via single nuclei combined ATAC/RNA

113 sequencing (10x Chromium Single Cell Multiome ATAC + Gene Expression). We profiled 13,622

114 single nuclei (5,669 naïve and 7,339 recovered) and identified major clusters based on chromatin

115 accessibility using Seurat [22] (Table S1). Most profiled nuclei were derived from macrophages

116 (65%) that clustered as two separate populations, followed by CD8 T cells (16%) (Figure 1B). In

4

117　accordance with flow cytometry data, CD8 T cells were primarily present in BALF of recovered

118　mice (Figure 1C). Intriguingly, macrophage clusters 1 and 2 were mainly driven by experimental

119　condition, with macrophage cluster 2 consisting almost exclusively of nuclei isolated from

120　recovered animals (Figure 1C). To compare epigenetic changes in recovered and naïve

121　macrophages following SARS2 infection, we extracted and re-clustered all putative macrophages

122　from the dataset, including myeloid cells (Figures 1S and S1I). Differentially regulated genes (DEG)

123　were enriched for gene ontology (GO) terms related to cytokine production and myeloid cell

124　differentiation for naïve and histone modification and chromatin organization in recovered

125　macrophages (Figure S1J). Yet, the transcriptomic profiles of recovered and naïve macrophages

126　were surprisingly comparable with only 36 of 5,701 detected genes being significantly regulated

127　by more than 1.4-fold between conditions (Figure S1K; Table S1). However, comparing chromatin

128　accessibility transcription factor (TF) binding motifs using chromVAR [23] revealed distinct

129　differences in recovered and naïve macrophages. Recovered macrophages showed increased

130　accessibility of TF binding motifs associated with antiviral immune response and type I interferon

131　(IFN-I) signaling, including interferon regulatory factors (IRFs) and signal transducer and activator

132　of transcription (STAT) proteins (Figure 1D). In contrast, accessibility of binding motifs associated

133　with nuclear factor kappa-light-chain-enhancer of activated B cell (NF-κB) was lower in recovered

134　macrophages (Figure 1D; Table S1). Immunofluorescence staining of airway-resident

135　macrophages *ex vivo* showed that recovered cells had increased nuclear levels of IRF3 but not

136　RELA (p65 subunit of NF-κB) relative to naïve cells (Figures 1E and S1L).

137　These data show that alveolar macrophages in mice retain epigenetic imprinting following SARS2

138　infection.

139

140　Past COVID-19 leads to establishment of epigenetic imprinting in circulating monocytes in

141　patients

142　To determine if an antiviral program persists in humans following SARS2 infection and clearance,

143　we recruited a patient cohort during the initial infection wave in 2020, prior to availability of

144　COVID-19 vaccines. We performed single nuclei combined ATAC/RNA sequencing on peripheral

145　blood mononuclear cells (PBMCs) isolated from patients recovered from mild COVID-19 after 2-

146   4 months (n = 3) and healthy controls (n = 7). Based on transcriptional profile, we identified major

147   cell clusters in PBMCs (Figure 2A). We focused our analyses on myeloid cell clusters (CD14+ and

148   CD16+ monocytes and dendritic cells (DCs)) and found increased expression of genes related to

149   the GO category "Defense Response to Virus" in recovered patients (Figures 2B and S2A, Table

150   S2). Although to a lesser extent, this gene module was also enriched in recovered murine

151   macrophages in BALF (Figure 2C). Gene module enrichment analyses of DEG in murine recovered

152   vs. naïve BALF macrophages (Figure S1I-S1K) underscored human CD14+ monocytes as suitable

153   cell population to analyze epigenetic memory in patients (Figures 2D and S2B). Consistent with

154   data obtained from murine macrophages in BALF, TF binding site accessibility was significantly

155   higher for IRFs and lower for NF-κB in CD14+ monocytes from recovered compared to healthy

156   patients (Figure 2E and Table S2).

157

158   Past SARS2 infection increases secondary antiviral immune responses in murine airway-resident

159   macrophages

160   To investigate whether SARS2-associated epigenetic imprinting alters secondary immune

161   responses, we isolated airway-resident macrophages from recovered and naïve animals and

162   stimulated them *ex vivo* with the synthetic viral double-stranded RNA mimic polyinosinic-

163   polycytidylic acid (polyIC). Upon polyIC stimulation, recovered macrophages displayed

164   significantly higher levels of nuclear IRF3 than naïve macrophages (Figure 3A). At the

165   transcriptional level, control and polyIC-stimulated recovered and naïve macrophages clustered

166   by stimulation and infection history (Figure S3A). We identified 2,654 DEG and hierarchical

167   clustering revealed both infection history-specific gene sets (clusters 1 and 6) and polyIC

168   response genes, including interferon-stimulated genes (ISGs) [24] (cluster 2) (Figure 3B; Table S3).

169   Genes associated with naïve cells were enriched for GO terms related to lipid and cholesterol

170   metabolism (Figure 3C), whereas recovered cells expressed genes related to macrophage

171   activation and inflammatory response (Figure 3D). Cluster 2 was enriched for GO terms related

172   to antiviral immunity and interferon response (Figure 3E). Recovered macrophages exhibited a

173   pronounced hyperresponsiveness to polyIC, characterized by robust induction of ISGs, including

174   *Ifit1*, *Ifitm3*, *Bst2* (Figures S3B-S3D; Table S3). As a functional consequence, recovered

175   macrophages were significantly less susceptible to infection with vesicular stomatitis virus

176   expressing a GFP reporter (VSV-GFP) compared to naïve macrophages (Figure 3F). These findings

177   suggest that SARS2-associated epigenetic imprinting of airway-resident macrophages results in

178   innate immune memory that augments subsequent antiviral immune responses.

179

180   Viral PAMP encounter is sufficient to establish antiviral innate immune memory in primary

181   alveolar macrophages and requires canonical IFN-I signaling

182   To explore these findings using a tractable *in vitro* system, we employed a long-term culture

183   system of primary alveolar macrophages [25]. We exposed alveolar macrophages to polyIC for 24h

184   and then re-stimulated them with polyIC after 5 days. Alveolar macrophages that previously

185   experienced polyIC showed significantly increased nuclear IRF3 levels upon restimulation with

186   polyIC (polyIC/polyIC) compared to control-experienced cells (control/polyIC) (Figure 4A). Like

187   SARS2-experienced alveolar macrophages, we did not observe significant differences in nuclear

188   localization of RELA (p65) (Figure S4A). Differential transcriptomic analyses confirmed a

189   significantly more robust antiviral recall response (Figures 4B and 4C; Table S4) and ISG induction

190   (*Ifit1*, *Ifitm3* and *Bst2*) (Figures S4B-S4D) in polyIC/polyIC vs. control/polyIC cells. Functionally,

191   this correlated with a 17-fold increased resistance to infection with VSV-GFP as assayed after 5

192   days and was maintained up to 14 days, albeit to a lesser extent (Figures S4E and S4F). Memory

193   formation required IFN-I signaling during initial polyIC exposure (Figure 4D) and the canonical

194   downstream transcription factor IRF9 (Figure 4E). Mice that received polyIC-experienced alveolar

195   macrophages 3 days prior to infection showed significantly ameliorated body weight loss upon

196   infection with influenza A/PR/8/34 virus (PR8) (Figure 4F). Thus, like SARS2 infection *in vivo*,

197   polyIC exposure *in vitro* leads to innate immune memory formation in alveolar macrophages that

198   is sufficient to ameliorate pathology of a viral infection *in vivo*.

199

200   Past SARS-CoV-2 infection can ameliorate the pathology of secondary influenza A virus infection

201   Finally, we investigated whether innate immune memory following SARS2 infection affects

202   disease pathology caused by a heterologous respiratory virus. We challenged naïve or SARS2-

203   recovered animals with a sub-lethal dose of PR8 (naïve/PR8 and SARS2/PR8, respectively) and

204 found significantly reduced body weight loss in SARS2/PR8 animals (Figure S5A). Likewise, past

205 SARS2 infection ameliorated body weight loss and reduced lethality using a higher (LD50)

206 infectious dose of PR8 (Figures 5A and 5B). Immune cell profiling of BALF revealed significantly

207 reduced neutrophil numbers in the SARS2/PR8 group but showed no significant differences in

208 alveolar macrophages or NK cell numbers (Figures 5C-5E). Increased CD8 T cell numbers in SARS2-

209 recovered animals (Figure S5H) were maintained in the early phase of PR8 infection (3dpi), but

210 not at later time points (Figure 5F). Hyperinflammatory responses in the airway are the major

211 determinant of lethal influenza infection [26]. Several pro-inflammatory cytokines and chemokines

212 (IL-1β, IL-17, CCL4 and CCL12) were significantly reduced in BALF of SARS2/PR8 compared to

213 naïve/PR8 animals at 5 dpi (Figure 5G), suggesting that past SARS2 infection limits dysregulated

214 inflammatory responses. Notably, there was no significant difference in viral RNA levels in lung

215 tissue between naïve/PR8 and SARS2/PR8 animals (Figure S5B).

216 To identify cell type-specific and cell-intrinsic differences associated with secondary infection, we

217 performed single cell RNA-seq (scRNA-seq) of naïve/PR8 and SARS2/PR8 BALF at 7dpi. We

218 sequenced 12,032 single cells (5,004 naïve/PR8 and 7,028 SARS2/PR8) and identified major cell

219 clusters in which the majority were macrophages (40%), followed by CD8 T cells (18%) (Figure

220 5H). Macrophages separated into clusters 1 (82%) and 2 (18%) characterized by increased

221 antiviral immunity and fatty acid metabolism, respectively (Figure S5C; Table S5). Cells in

222 macrophage cluster 1 and neutrophils expressed particularly high levels of ISGs (Figure S5D).

223 Within those clusters, DEG analyses revealed significantly increased expression of antiviral genes

224 in cells isolated from SARS2/PR8 compared to naïve/PR8 animals (Figures 5I and S5E; Table S5).

225 DEG in CD8 T cells were enriched for GO terms related to T cell differentiation and RNA

226 metabolism (SARS2/PR8) and oxidative phosphorylation and ATP metabolism (naïve/PR8),

227 suggesting no antigen-independent bystander activation of SARS2-specific cells in SARS2/PR8

228 animals (Figure S5F; Table S5). These data highlight a beneficial effect of past SARS2 infection on

229 disease pathology caused by the heterologous pathogen influenza A PR8.

230

231

232

Discussion

Antigen-independent, innate immune memory alters secondary inflammatory responses. Consequently, heterologous pathogens can indirectly influence each other, including emerging pathogens [4].

Innate immune memory can be established locally or centrally. Systemic exposure to PAMPs can result in epigenetic imprinting of immune progenitor cells in the bone marrow and central innate immune memory that facilitates tissue cross-protection [6,7,27–29]. Further, innate immune memory mounted by long-lived stem cells can provide extended longevity compared to short-lived effector immune cells [5,30]. There is evidence of durable epigenetic memory in hematopoietic stem and progenitor cells and circulating monocytes from human patients following severe SARS-CoV-2 infection and hospitalization that translates to altered secondary responses [31]. Yet, pre-clinical animal models are critical to investigate the quality and breadth of SARS-CoV-2-induced innate immune memory – particularly at the tissue level and in the context of mild disease. The murine infection model of SARS-CoV-2 strain MA10 recapitulates many features of COVID-19 in humans [20]. We discovered that past SARS-CoV-2 infection induces local innate immune memory via epigenetic imprinting of airway-resident macrophages. Alveolar macrophages form a self-renewing macrophage population of the airway that maintains itself throughout life at an estimated cell division rate of more than 2 weeks [16,32]. Hence, epigenetic remodeling in airway-resident macrophages may contribute to the establishment of sustained, local innate immune memory. Of note, severe lung injury can coincide with depletion of alveolar macrophages that are sustainably replenished by infiltrating monocytes [15,33]. These monocyte-derived alveolar macrophages can display an inflammatory phenotype and contribute to innate immune memory on a population level [34,35].

Following SARS-CoV-2, epigenetic memory of airway-resident macrophages was strongly skewed towards increased chromatin accessibility of IRF-related transcription factors. This allowed enhanced and rapid secondary antiviral responses, limiting detrimental hyperinflammatory responses in secondary influenza virus A infection. Epigenetic and transcriptional profiling of myeloid cells in a cohort comprised of healthy individuals and patients recovered from mild

262   COVID-19 before availability of COVID-19 vaccine corroborated these findings. Consistent with

263   our observations, circulating CD14^{+} monocytes from individuals who received a trivalent seasonal

264   influenza vaccine exhibited increased chromatin accessibility for IRFs and antiviral gene

265   expression [36].

266

267   Next to epigenetic imprinting, recovered macrophages retained an altered metabolic

268   transcriptional program that suggests reduced activity of fatty acid metabolism. A similar

269   metabolic switch is associated with increased inflammatory responses of immune cells [37–39] and

270   is in agreement with increased glycolytic activity of alveolar macrophages in adenovirus-

271   recovered animals [8]. Interestingly, altered secondary immune responses of LPS-experienced

272   alveolar macrophages seem to depend on fatty acid oxidation rather than glycolysis [18].

273   Similar to bacterial PAMP exposure [18,40], the synthetic viral dsRNA mimic polyIC was sufficient to

274   establish innate immune memory in alveolar macrophages that depended on canonical IFN-I

275   signaling and the downstream TF IRF9. This aligns with our finding of increased chromatin

276   accessibility of the IRF9 binding motif in airway-resident macrophages following SARS-CoV-2

277   infection. Some studies suggest that IFN-I is sufficient to establish epigenetic memory, but

278   appears to be more robust in immune cells compared to fibroblasts [18,41]. Exposure of alveolar

279   macrophages to polyIC led to increased secondary antiviral responses *in vitro* and ameliorated

280   disease caused by influenza A virus *in vivo*. These findings show that viral PAMP recognition can

281   lead to formation of innate immune memory in alveolar macrophages that is sufficient to

282   influence pathology of secondary respiratory viral infections. Our description of matching

283   epigenetic antiviral imprinting in myeloid cells of recovered COVID-19 patients implies that these

284   shared programs might broadly modulate human responses to subsequent infections.

285

286   Further, innate immune memory in macrophages can impact on other immune cells and shape

287   adaptive T cell responses [8,42]. While we did not observe pronounced differences in T cell

288   recruitment and transcriptional profile between SARS2/PR8 and naïve/PR8 animals, we found

289   increased ISG expression in alveolar macrophages and neutrophils. These data suggest that

290   alveolar macrophages in SARS2/PR8 animals retain elevated antiviral activity during the acute

291 phase of PR8 infection. Increased expression of ISGs in recruited neutrophils may be a secondary

292 effect resulting from disparate inflammatory conditions in the airways of naïve/PR8 and

293 SARS2/PR8 animals.

294

295 Innate immune memory can be pro-inflammatory or tolerogenic which is thought to be primarily

296 determined by initial PAMP encounter [43]. Increased LPS levels dampen secondary inflammatory

297 responses in monocytes [43,44]. In line with this, monocytes of sepsis-recovered patients displayed

298 immune paralysis and impaired phagocytic activity [45]. While these tolerogenic recall responses

299 are detrimental in certain secondary diseases, including cancer [46], they might also foster microbe-

300 host co-existence and limit immunopathology [47]. LPS-induced tolerance in monocytes can be

301 reverted by subsequent exposure to the fungal PAMP β-glucan [44]. This highlights a therapeutic

302 opportunity, but also emphasizes that crosstalk between distinct inflammatory cues shapes the

303 quality of innate immune memory in a cell-autonomous fashion. Likewise, the nature of

304 secondary inflammatory signals influences the robustness of recall responses. Previous BCG

305 encounter ameliorates disease caused by the respiratory pathogen influenza A virus but not

306 SARS-CoV-2 and might be linked to differences in pulmonary vasculature damage and pathogen

307 dissemination [28]. These observations highlight innate immune memory as a complex dynamic

308 trait. Especially in the context of infectious diseases, individual contributions and interplay of

309 pathogen, host immune response, tissue damage and cellular heterogeneity remain incompletely

310 understood [8,18,19,33,35,40]. Well-controlled clinically relevant model systems are key to

311 systematically dissect the interplay of inflammatory cues shaping the quality of innate immune

312 memory.

313

314 Innate immune memory is not limited to infectious diseases but is also established in

315 autoimmune disorders. Chronic rhinosinusitis in humans leads to epigenetic remodeling in basal

316 stem cells of the upper airway that impacts inflammatory responses [48]. Allergic asthma causes

317 inflammatory imprinting in macrophages that exacerbates disease in a TNF-dependent fashion

318 [49]. Further, tissue crosstalk in autoimmune-induced innate immune memory can shape pathology

319 of arthritis following recovery from periodontitis [50]. There is a gap of knowledge regarding the

320   crosstalk of pathogen and autoimmune-associated innate immune memory, as well as the

321   reciprocal influence of disease pathology.

322

323   This study shows that past SARS-CoV-2 infection leads to establishment of epigenetic memory of

324   airway-resident macrophages. Formation of innate immune memory depended on viral PAMP

325   sensing and IFN-I signaling. This promoted increased secondary antiviral responses that

326   translated to ameliorated pathology caused by subsequent challenge with influenza A virus. One

327   can imagine that in the real-world onslaught of respiratory pathogens, the induction and duration

328   of antigen-independent innate immune memory, along with the timing and nature of pathogen

329   exposure, will have significant impact on infection outcome.

330

331   **Acknowledgements**

332   The authors would like to thank Roni Winkler, Michael Bauer, Margaret MacDonald, Shira

333   Weingarten-Gabbay, Tyler Lewy, Hsuan-An Chen, Mariana Nogueira Batista and the Rice lab for

334   valuable input on experimental design, data interpretation and feedback on the manuscript. We

335   thank Ralph Baric for sharing the mouse-adapted SARS-CoV-2 strain MA10 and the Flow

336   Cytometry Resource Center at Rockefeller University for technical support.

337

338   **Data availability**

339   RNA sequencing and 10x Multiome data will be made publicly available once the manuscript is

340   published.

341

342   **Conflict of interest**

343   The authors declare no conflict of interest.

344

345   **Author contributions**

346   A.L. and C.M.R. wrote the manuscript. A.L. designed and performed *in vivo* and *in vitro* studies.

347   A.L., J.G.C., B.R.R. performed bioinformatic analyses. C.J., H.H.H., A.W.A., Y.S.Y., E.J.D. performed

348   *in vitro* studies. C.Q. supported the *in vivo* studies. L.C. performed histological analyses. A.L.,

349   B.R.R., S.Z.J., C.M.R. designed and analyzed experiments. C.M.R. supervised the study. All co-

350   authors provided feedback on the manuscript.

351

352

353   **Funding**

354   Research reported in this publication received funding from the National Institute of Allergy and

355   Infectious Diseases (NIAID) of the National Institutes of Health (NIH) under award number

356   R01AI161444 awarded to C.M.R., R01AI151029, U01AI150748 warded to B.R.R. and

357   R01AI148416, R01AI148416-S1, R01AI148416-S2 awarded to S.Z.J. A.L. was supported by a long-

358   term postdoctoral fellowship awarded by the Human Frontiers Science Program (HFSP) under

359   award number LT000203/2021-L. J.G.C. was supported by a scholarship awarded by the Asan

360   Foundation.

361

362

363
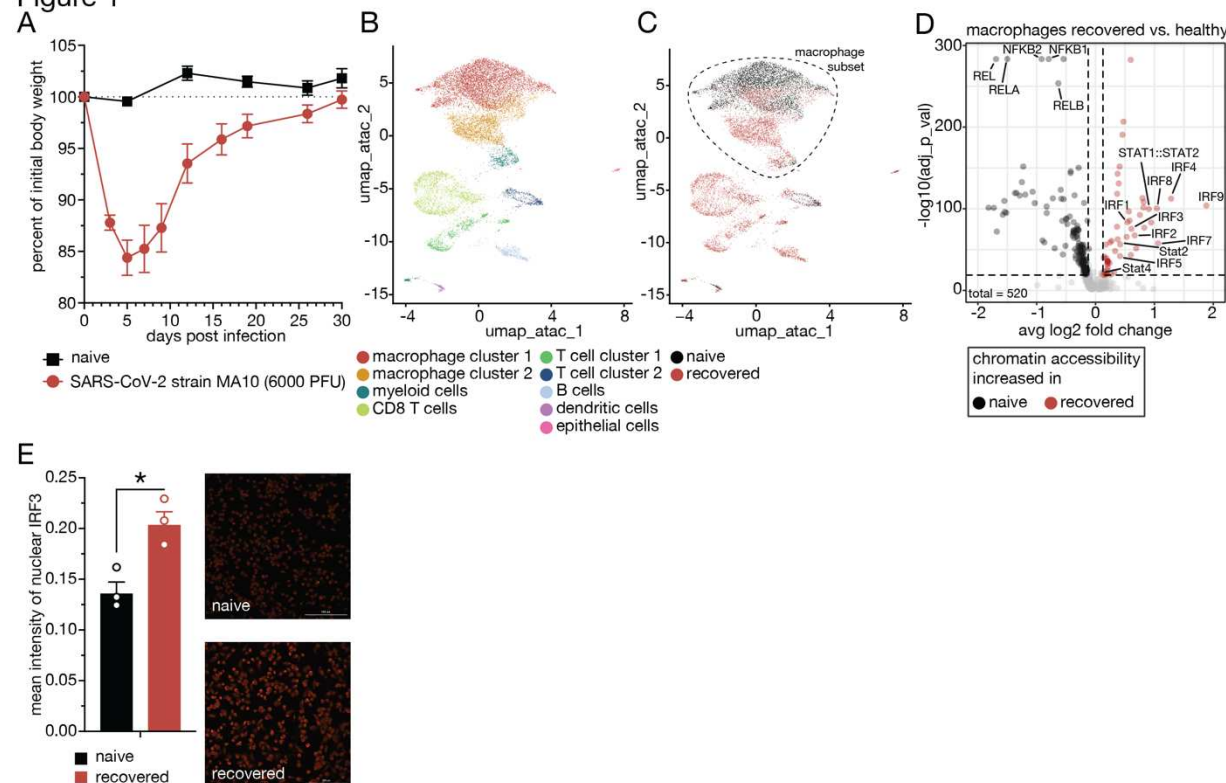
364 **Figures**

365

Figure 1

Figure 1: Past SARS-CoV-2 infection establishes epigenetic memory in airway-resident macrophages.
(A) Body weights of naïve and SARS-CoV-2 (strain MA10) infected C57Bl/6J mice. n = 11-12. (B) UMAP clustering of single nuclei combined ATAC/RNA-seq data (10x Multiome) and annotated cell clusters of airway-resident cells from naïve and SARS-CoV-2-recovered mice based on ATAC-seq data. n = 3. (C) Recovered and naïve sample annotation of UMAP clustering (B) with dashed line indicating the macrophage subset. (D) TF motif-associated chromatin accessibility analyses of recovered vs. naïve sub-setted macrophages. (E) Quantification of mean fluorescent intensity of nuclear IRF3 in airway-resident macrophages isolated from naïve and SARS-CoV-2-recovered animals and representative image. n = 3. Data are mean ± s.e.m. n values indicate the number of mice or replicates. For (D), statistical analysis was performed using Wilcoxon's test. For (E), statistical analysis was performed using Student's t-test with Bonferroni correction when multiple comparisons were performed. *p < 0.05; **p < 0.01; ***p < 0.001.
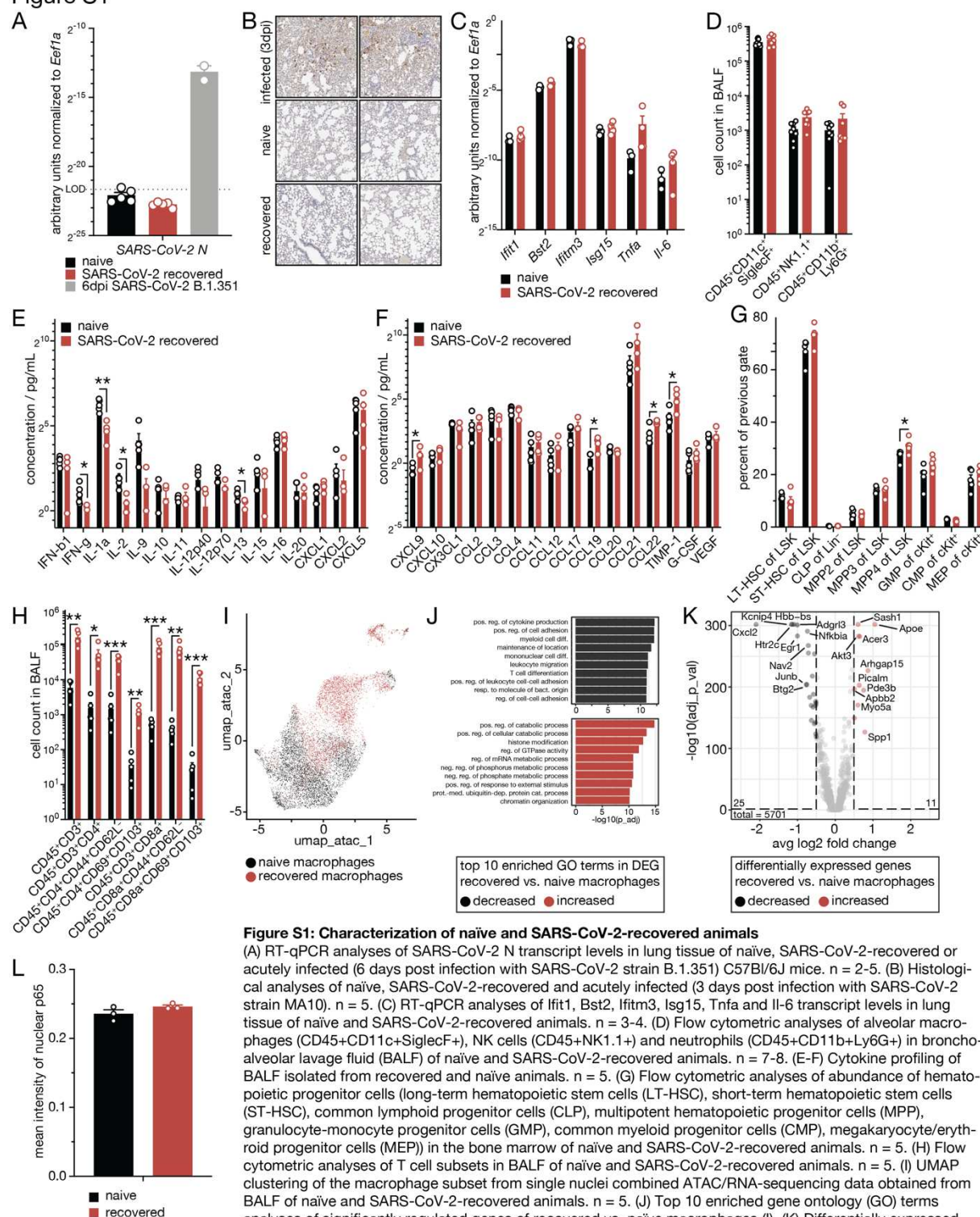
366

367

14

Figure S1

Figure S1: Characterization of naïve and SARS-CoV-2-recovered animals

(A) RT-qPCR analyses of SARS-CoV-2 N transcript levels in lung tissue of naïve, SARS-CoV-2-recovered or acutely infected (6 days post infection with SARS-CoV-2 strain B.1.351) C57Bl/6J mice. n = 2-5. (B) Histological analyses of naïve, SARS-CoV-2-recovered and acutely infected (3 days post infection with SARS-CoV-2 strain MA10). n = 5. (C) RT-qPCR analyses of Ifit1, Bst2, Ifitm3, Isg15, Tnfa and Il-6 transcript levels in lung tissue of naïve and SARS-CoV-2-recovered animals. n = 3-4. (D) Flow cytometric analyses of alveolar macrophages (CD45+CD11c+SiglecF+), NK cells (CD45+NK1.1+) and neutrophils (CD45+CD11b+Ly6G+) in bronchoalveolar lavage fluid (BALF) of naïve and SARS-CoV-2-recovered animals. n = 7-8. (E-F) Cytokine profiling of BALF isolated from recovered and naïve animals. n = 5. (G) Flow cytometric analyses of abundance of hematopoietic progenitor cells (long-term hematopoietic stem cells (LT-HSC), short-term hematopoietic stem cells (ST-HSC), common lymphoid progenitor cells (CLP), multipotent hematopoietic progenitor cells (MPP), granulocyte-monocyte progenitor cells (GMP), common myeloid progenitor cells (CMP), megakaryocyte/erythroid progenitor cells (MEP)) in the bone marrow of naïve and SARS-CoV-2-recovered animals. n = 5. (H) Flow cytometric analyses of T cell subsets in BALF of naïve and SARS-CoV-2-recovered animals. n = 5. (I) UMAP clustering of the macrophage subset from single nuclei combined ATAC/RNA-sequencing data obtained from BALF of naïve and SARS-CoV-2-recovered animals. n = 5. (J) Top 10 enriched gene ontology (GO) terms analyses of significantly regulated genes of recovered vs. naïve macrophages (I). (K) Differentially expressed genes (DEG, absolute log2 fold change > 0.5) in macrophages (I) of recovered and naïve animals. Top 10 significant DEG by fold change are labelled. (L) Quantification of mean fluorescent intensity of nuclear RELA (p65) in airway-resident macrophages isolated from naïve and SARS-CoV-2-recovered animals. n = 3. Data are mean ± s.e.m. n values indicate the number of mice or replicates. For (A, C-H and L), statistics were calculated using Student's t-test with Bonferroni correction when multiple comparisons were performed. For (K), statistical analysis was performed using Wilcoxon rank sum test with Bonferroni correction. For (J), hypergeometric p values were adjusted for multiple testing with Benjamini-Hochberg correction. *p < 0.05; **p < 0.01; ***p < 0.001.
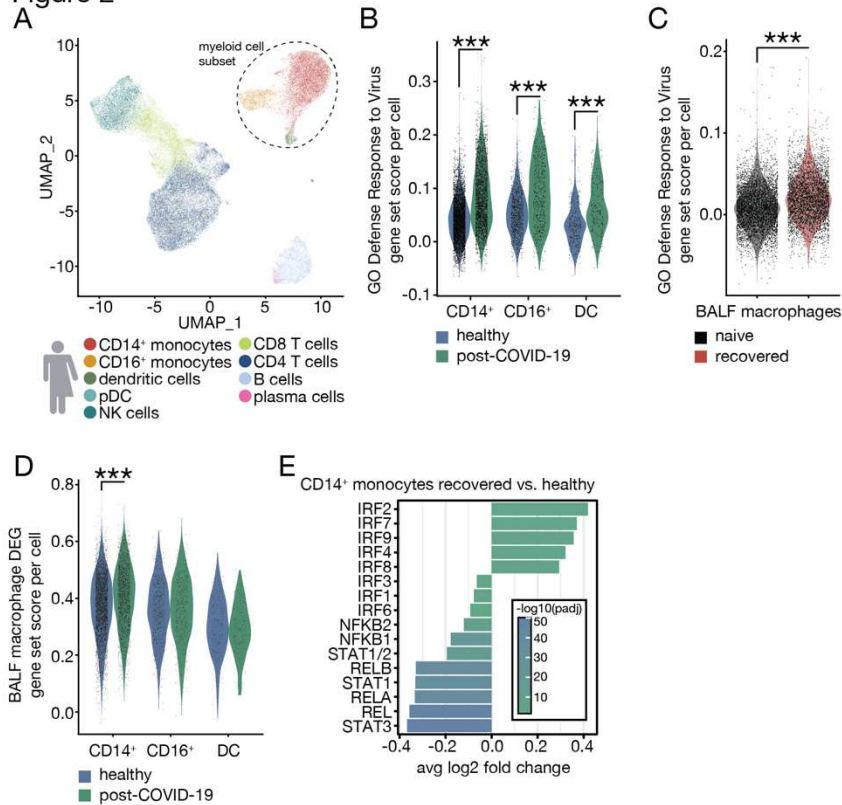
368

Figure 2

Figure 2: Past COVID-19 establishes epigenetic memory in circulating monocytes in patients.
(A) UMAP clustering of single nuclei combined ATAC/RNA-seq data and annotated cell clusters of peripheral blood mononuclear cells (PBMCs) of recovered (2-4 months) mild COVID-19 and healthy patients with dashed line indicating the myeloid cell subset. n = 3-7. (B–C) Gene set expression score of GO: Defense Response to Virus in recovered and healthy circulating human myeloid cells (CD14+ and CD16+ monocytes and dendritic cells) (B) and murine BALF macrophages (C). (D) Gene set expression score of differentially expressed gene (DEG) module in circulating human myeloid cells. (E) Significantly different accessible TF motif-associated chromatin of recovered vs. healthy CD14+ monocytes. Data are represented as violin plots with each dot corresponding to one individual cell. For (B-E), statistical analyses were performed using Wilcoxon's test. *p < 0.05; **p < 0.01; ***p < 0.001.

369

Figure S2

Figure S2: Characterization of naïve and SARS-CoV-2-recovered patient PBMCs
(A) Gene set expression score of GO: Defense Response to Virus across all recovered and healthy circulating human myeloid cells. (B) Expression of BALF cluster signature genes and macrophage subset (Figure 1I) differentially expressed gene (DEG) modules in circulating human myeloid cells (CD14+ and CD16+ monocytes and dendritic cells). Data are represented as violin plots or dotplot with each dot corresponding to one individual cell or cell cluster, respectively. For (A-B), statistical analysis was performed using Wilcoxon rank sum test with Bonferroni correction. *p < 0.05; **p < 0.01; ***p < 0.001.

370

Figure 3: Past SARS-CoV-2 infection leads to increased secondary antiviral responses in airway-resident macrophages.
(A) Quantification of mean fluorescent intensity (MFI) of IRF3 in control– or polyIC-stimulated airway-resident macrophages isolated from naïve and SARS-CoV-2-recovered animals after 24 hours. n = 3. (B) Hierarchical clustering of differentially expressed genes (DEG) of control– or polyIC-stimulated airway-resident macrophages isolated from naïve or SARS-CoV-2-recovered animals after 6 hours. n = 3. (C-E), Gene ontology (GO) enrichment analyses of genes in clusters 1 (C), 6 (D), 2 (E). (F) Percent of VSV-GFP infected airway-resident macrophages isolated from naïve or SARS-CoV-2-recovered animals. n = 3. For (A and F), statistics were calculated using Student's t-test with Bonferroni correction when multiple comparisons were performed. For (C-E), hypergeometric p values were adjusted for multiple testing with Benjamini-Hochberg correction. *p < 0.05; **p < 0.01; ***p < 0.001.

371

Figure S3

Figure S3: Characterization of secondary response of airway-resident macrophages isolated from naïve and SARS-CoV-2-recovered animals

(A) Principal component analyses of transcriptomic profile of control– or polyIC-stimulated airway-resident macrophages isolated from naïve or SARS-CoV-2-recovered animals. n = 3. (B-D), RT-qPCR analyses of Ifit1 (B), Ifitm3 (C) and Bst2 (D) transcript levels in control– or polyIC-stimulated airway-resident macrophages isolated from naïve or SARS-CoV-2-recovered animals. n = 3. Data are mean ± s.e.m. n values indicate the number of mice or replicates. For (B-D), statistics were calculated using Student's t-test with Bonferroni correction when multiple comparisons were performed. *p < 0.05; **p < 0.01; ***p < 0.001.

372

Figure 4: Viral PAMP exposure is sufficient to establish innate immune memory in alveolar macrophages in vitro.
(A) Quantification of mean fluorescent intensity (MFI) of IRF3 in control– or polyIC-stimulated control– or polyIC-experienced in vitro cultured alveolar macrophages after 24 hours. n = 4. (B) Hierarchical clustering of differentially expressed genes (DEG) of polyIC/polyIC vs. control/polyIC alveolar macrophages 6 hours after re-stimulation. n = 3. (C) Gene ontology (GO) enrichment analyses of genes in clusters 2. (D) Percent of VSV-GFP infected control– or polyIC-experienced alveolar macrophages with or without anti-IFNAR blocking antibody treatment during initial polyIC exposure. n = 4. (E) Percent of VSV-GFP infected control– or polyIC-experienced wild type or Irf9–/– alveolar macrophages. n = 4. (F) Body weights of influenza A/PR/8/34 virus infected C57Bl/6J mice following transfer of control– or polyIC-experienced alveolar macrophages. n = 4. Data are mean ± s.e.m. n values indicate the number of mice or replicates. For (A), statistics were calculated using Student's t-test with Bonferroni correction when multiple comparisons were performed. For (C), hypergeometric p values were adjusted for multiple testing with Benjamini-Hochberg correction. For (D-E), statistical analysis was performed using Two-Way ANOVA comparison with Bonferroni correction. For (F), statistical analysis was performed using Two-Way ANOVA comparison with Bonferroni correction. *p < 0.05; **p < 0.01; ***p < 0.001.
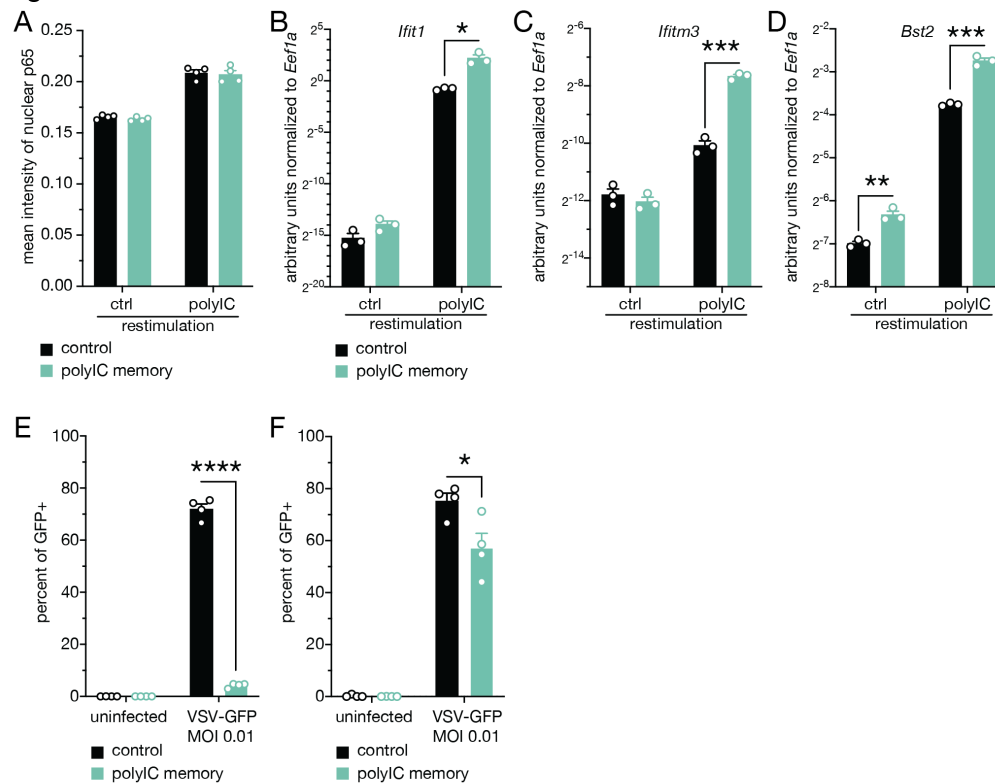
373

Figure S4

Figure S4: Characterization of secondary response of polyIC-experienced alveolar macrophages in vitro
(A) Quantification of mean fluorescent intensity of RELA (p65) in control– or polyIC-stimulated control– or polyIC-experienced in vitro cultured alveolar macrophages after 6 hours. n = 4. (B-D), RT-qPCR of Ifit1 (B), Ifitm3 (C) and Bst2 (D) transcript levels of polyIC/polyIC vs. control/polyIC stimulated in vitro cultured alveolar macrophages 6 hours after re-stimulation. n = 3. (E-F), Percent of VSV-GFP-infected control– or polyIC-stimulated control– or polyIC-experienced in vitro cultured alveolar macrophages after 5 (E) and 14 days (F). n = 4. Data are mean ± s.e.m. n values indicate the number of mice or replicates. For (A-F), statistics were calculated using Student's t-test with Bonferroni correction when multiple comparisons were performed. *p < 0.05; **p < 0.01; ***p < 0.001.
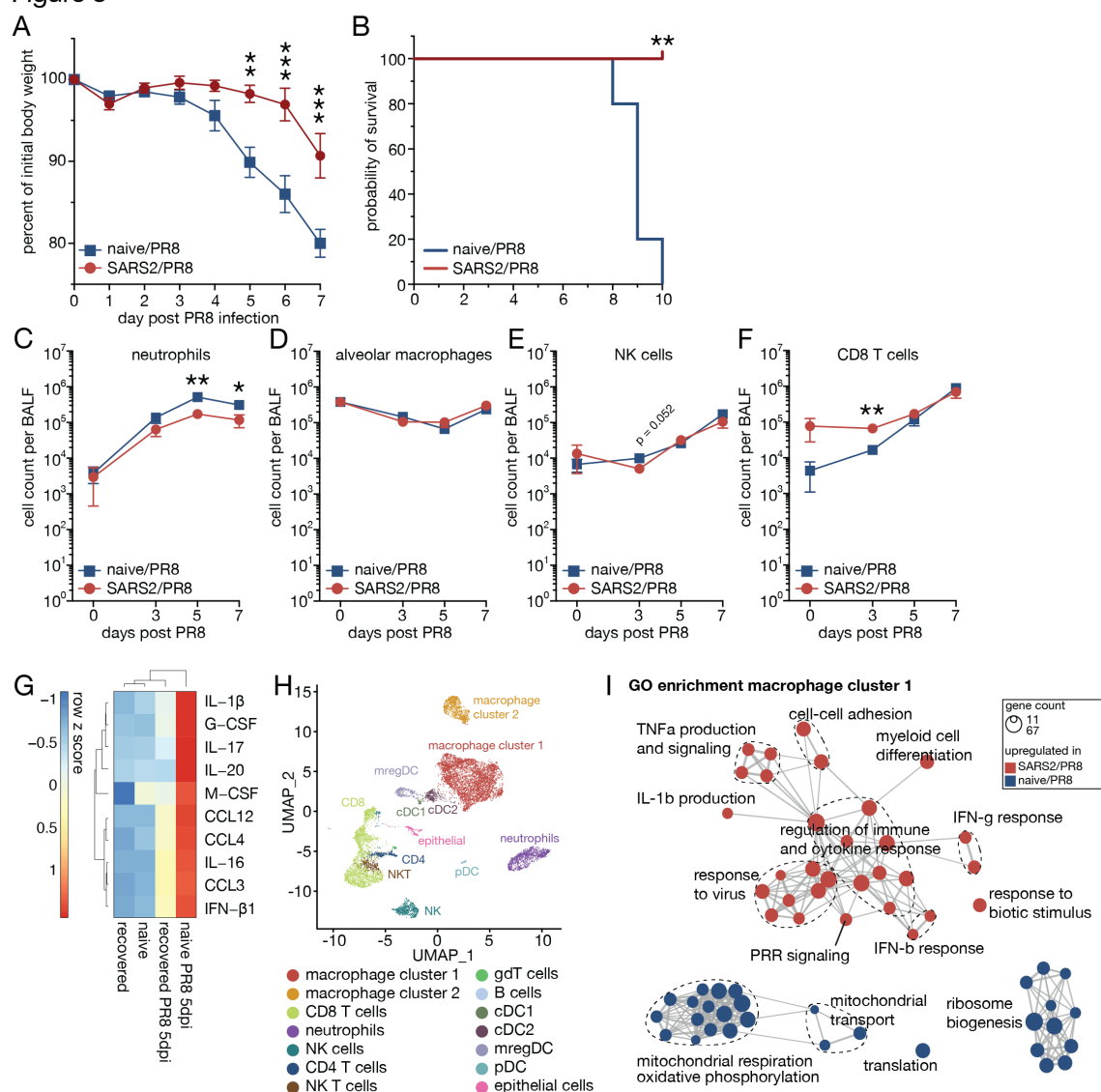
374

Figure 5

Figure 5: Past SARS-CoV-2 infection ameliorates secondary influenza A virus infection.
(A) Body weights of naïve and SARS-CoV-2-recovered animals infected with influenza A/PR/8/34 virus at LD50 (naïve/PR8 or SARS2/PR8). n = 5. (B) Survival percentages of naïve/PR8 and SARS2/PR8 animals. n = 5. (C-F) Kinetics of neutrophils (C), alveolar macrophages (D), NK cells (E) and CD8 T cells (F) in bronchoalveolar lavage fluid (BALF) of naïve/PR8 and SARS2/PR8 animals. n = 3-7. (G) Significantly different cytokines and chemokines in BALF of naïve/PR8 and SARS2/PR8 animals at 5 days after PR8 infection. n = 4-5. (H) UMAP clustering and major cell cluster annotation of single cell RNA-seq data of BALF from naïve/PR8 and SARS2/PR8 animals at 7 days post PR8 infection. (I) Gene ontology (GO) enrichment analyses of genes associated with cells isolated from naïve/PR8 or SARS2/PR8 BALF in macrophages cluster 1 (G). Data are mean ± s.e.m. n values indicate the number of mice or replicates. For (A), statistical analysis was performed using Two-Way ANOVA comparison with Bonferroni correction. For (B), statistical analysis was performed using a log-rank Mantel-Cox test. For (C-G), statistics were calculated using Student's t-test with Bonferroni correction when multiple comparisons were performed. For (I), hypergeometric p values were adjusted for multiple testing with Benjamini-Hochberg correction. *p < 0.05; **p < 0.01; ***p < 0.001.
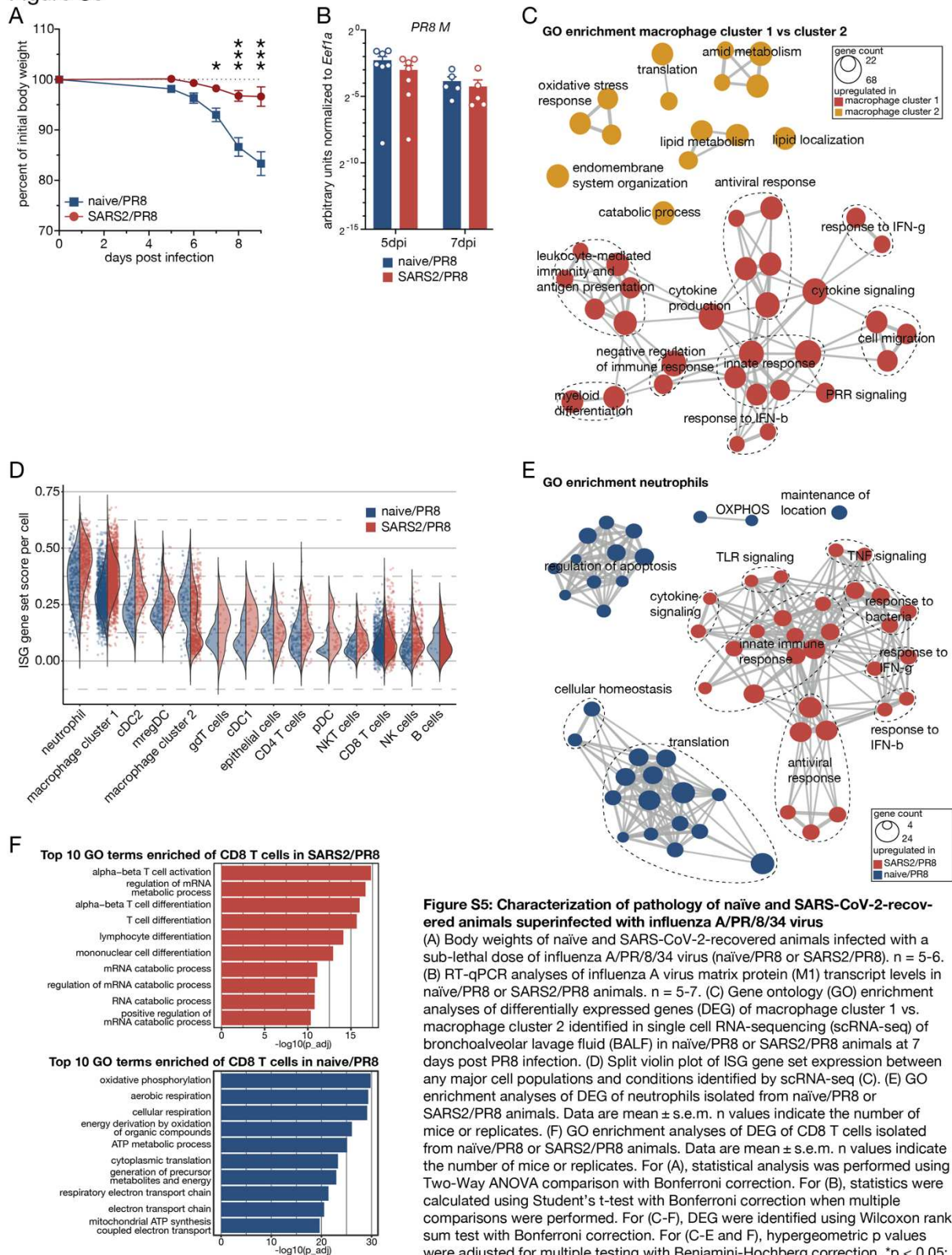
375

Figure S5

Figure S5: Characterization of pathology of naïve and SARS-CoV-2-recovered animals superinfected with influenza A/PR/8/34 virus

(A) Body weights of naïve and SARS-CoV-2-recovered animals infected with a sub-lethal dose of influenza A/PR/8/34 virus (naïve/PR8 or SARS2/PR8). n = 5-6. (B) RT-qPCR analyses of influenza A virus matrix protein (M1) transcript levels in naïve/PR8 or SARS2/PR8 animals. n = 5-7. (C) Gene ontology (GO) enrichment analyses of differentially expressed genes (DEG) of macrophage cluster 1 vs. macrophage cluster 2 identified in single cell RNA-sequencing (scRNA-seq) of bronchoalveolar lavage fluid (BALF) in naïve/PR8 or SARS2/PR8 animals at 7 days post PR8 infection. (D) Split violin plot of ISG gene set expression between any major cell populations and conditions identified by scRNA-seq (C). (E) GO enrichment analyses of DEG of neutrophils isolated from naïve/PR8 or SARS2/PR8 animals. Data are mean ± s.e.m. n values indicate the number of mice or replicates. (F) GO enrichment analyses of DEG of CD8 T cells isolated from naïve/PR8 or SARS2/PR8 animals. Data are mean ± s.e.m. n values indicate the number of mice or replicates. For (A), statistical analysis was performed using Two-Way ANOVA comparison with Bonferroni correction. For (B), statistics were calculated using Student's t-test with Bonferroni correction when multiple comparisons were performed. For (C-F), DEG were identified using Wilcoxon rank sum test with Bonferroni correction. For (C-E and F), hypergeometric p values were adjusted for multiple testing with Benjamini-Hochberg correction. *p < 0.05; **p < 0.01; ***p < 0.001.

376

23

Material and methods

Mice

C57Bl/6J wild type mice were obtained from the Jackson Laboratory (strain #000664). *Irf9*$^{-/-}$ mice (RBRC00916) [51] were obtained from Riken Bioresource Center, Japan. Mice were maintained and bred at the AAALAC-accredited Comparative Bioscience Center of the Rockefeller University. All mouse experiments were in accordance with the NIH Guide for the Care and Use of Laboratory Animals and approved by the Institutional Animal Care and Use Committee of Rockefeller University. Four- to six-month-old mice of both sexes were used for SARS-CoV-2 strain MA10 infection experiments. For all other experiments, adult mice (older than 2 months) of both sexes were used. For survival studies, body weight loss greater than 20% of initial weight was defined the humane endpoint. All SARS-CoV-2 animal experiments and downstream processing of live cells non-inactivated tissues were conducted under biosafety level 3 (BSL-3) containment in compliance with institutional and federal guidelines.

Cell lines

VeroE6 cells (*Chlorocebus sabaeus*; sex: female, kidney epithelial) obtained from the ATCC (CRL-1586) and Ralph Baric (University of North Carolina at Chapel Hill), and Huh-7.5 hepatoma cells (*Homo sapiens*; sex: male, liver epithelial) [52] were cultured in Dulbecco's Modified Eagle Medium (DMEM, Thermo Fisher Scientific #11995065) supplemented to contain 1 % non-essential amino acids (NEAA, Thermo Fisher Scientific #11140076) and 10 % fetal bovine serum (FBS, HyClone Laboratories, Lot. #AUJ35777). BHK-21 cells (*Mesocricetus auratus*, sex: male, fibroblast) were obtained from ATCC (#CCL-10) and MDCK cells (*Canis familiaris*, sex: female, kidney epithelial) were obtained from ATCC (#CCL-34) and cultured in Modified Eagle Medium (MEM, Thermo Fisher Scientific #11095080) supplemented to contain 10 % FBS, 1% Penicillin-Streptomycin (Thermo Fisher Scientific #15140122) and 1% L-Glutamine (Thermo Fisher Scientific #A2916801). All cell lines were cultured at 37 °C and 5 % CO_2. All cell lines were confirmed to be negative for mycoplasma contamination.

24

406 <u>Viruses</u>

407 *Influenza A/PR/8/34 virus*

408 Influenza A/PR/8/34 virus (IAV PR8) stocks were generated using 9-day-old embryonated chicken

409 eggs (Charles River #10100335). Eggs were incubated over night at 37 °C and candled by holding

410 the eggs directly against a light source to identify an inoculation site without any veins above the

411 air sac. The egg was inoculated with 1,000 plaque forming units (PFU) diluted in Dulbecco's

412 phosphate buffered saline (PBS, Thermo Fisher Scientific #14190144) + 1% BSA (Sigma Aldrich

413 #A9576) using a 18G needle. Eggs were incubated for 2 days at 37 °C and transferred to 4 °C for

414 2 hours. Next, eggs were opened with a sterile spoon and a scoopula was used to push down the

415 embryo and the allantoic fluid was collected. The allantoic fluid was centrifuged using an Allegra

416 X-12R (Beckman Coulter) at 205 G for 5 min, the supernatant was transferred into a clean falcon

417 tube and stored at -80 °C.

418 *VSV-GFP*

419 GFP-tagged vesicular stomatitis virus (VSV-GFP) [53] was generated by infecting 80% confluent BHK-

420 21 cells (ATCC #CCL-10) at a multiplicity of infection (MOI) of 0.01 PFU/cell. Cells were cultured

421 at 37 °C and cell culture supernatant was harvested after 2 days, clarified by centrifugation at

422 1,850 G for 5 min, and filtered through a 0.22 µm membrane and stored at -80 °C.

423 *SARS-CoV-2 strain MA10*

424 Severe acute respiratory syndrome coronavirus 2 (SARS-CoV-2) strain MA10 [20]

425 was generously provided by Ralph Baric (University of North Carolina at Chapel Hill). A P1 stock

426 was amplified in VeroE6 cells obtained from the ATCC that were engineered to stably express

427 TMPRSS2 (VeroE6$_{TMPRSS2}$). To generate a P2 working stock, VeroE6$_{TMPRSS2}$ cells were infected at a

428 multiplicity of infection (MOI) of 0.1 PFU/cell and incubated at 37 °C for 4 days. The virus-

429 containing supernatant was harvested, clarified by centrifugation at 1,850 G for 5 min for 10 min,

430 and filtered through a 0.22 µm membrane and stored at -80 °C.

431

432 <u>Plaque assay</u>

433 *Influenza A/PR/8/34 virus*

25

434   IAV PR8 was titrated by plaque assay on MDCK cells (ATCC #CCL-34) in 6-well format. Briefly,

435    $5x10^5$ cells per well were plated the day prior, medium was aspirated, and cells were washed

436   with PBS (Thermo Fisher Scientific #14190144) before 500 µL of a serial dilution of viral inoculum

437   in infection medium (RPMI, 0.1 % fetal bovine serum (FBS), 1 % Penicillin-Streptomycin, 0.3 %

438   BSA, 1 µg/mL tosylamido phenylalanyl chloromethyl ketone (TPCK)-treated trypsin) was added.

439   Cells were incubated for 60 min at 37 °C and plates were moved every 20 min to prevent drying

440   out of the wells. The initial inoculum was removed, 2 mL of overlay were added per well (25 mL

441   2x DMEM, 0.05 mL FBS, 15 mL 2% oxoid agar (Thermo Fisher Scientific #LP0011B), 0.5 mL 30 %

442   BSA, 0.5 mL 1 % diethylaminoethyl (DEAE)-dextran, 0.75 mL sodium bicarbonate ($NaHCO_3$), 0.05

443   mL 1mg/mL TPCK trypsin, 8.15 mL water) and cells were incubated at 37 °C for 2 days. Cells were

444   fixed by adding 2 mL 4 % paraformaldehyde (Sigma Aldrich #F8775) for 1 hour, the overlay was

445   removed, and cells were permeabilized by incubating with 1 mL 0.1% Triton X-100 (Sigma Aldrich

446   #93443) in PBS for 10 min at room temperature. Cells were washed 2 times with PBS, and

447   incubated with 500 µL of anti-IAV nucleoprotein (NP) antibody (1:3000, Sigma Aldrich

448   #MAB8257) in 5 % goat serum (Jackson Immuno Research #005-000-121) for 1 hour at 37 °C.

449   Cells were washed 2 times with 0.05 % Tween-20 (Sigma Aldrich P1379) in PBS, and incubated

450   with 500 µL anti-mouse-horseradish peroxidase (HRP) antibody (1:1000, Jackson Immuno

451   Research #115-035-146) in 0.05 % Tween-20 in PBS at 37 °C for 1 hour. Next, cells were washed

452   2 times with 0.05 % Tween-20 in PBS, add 500 µL KPL TrueBlue Peroxidase Substrate (Seracare

453   #5510-0052) and incubated for 1 min at room temperature. Cells were washed with PBS and viral

454   titer was quantified by enumerating foci.

455   *VSV-GFP*

456   VSV-GFP was titrated by plaque assay on BHK-21 cells (ATCC #CCL-10) in 6-well format. Briefly,

457    $5x10^5$ cells per well were plated the day prior, medium was aspirated and 500 µL before a 10-fold

458   serial dilution of viral inoculum was added. Cells were incubated for 60 min at 37 °C and plates

459   were moved every 20 min to prevent drying out of the wells. The initial inoculum was removed,

460   2 mL of overlay were added per well (25 mL 2x DMEM, 10 mL FBS, 15 mL 2% oxoid agar) and

461   incubated for 2 days at 37 °C. Cells were fixed by adding 2 mL 4 % paraformaldehyde (Sigma

462   Aldrich #F8775) for 1 hour at room temperature. The overlay was removed, and virus was

463   quantified by enumerating GFP-positive foci and/or upon adding crystal violet solution (1.25 %

464   crystal violet, 20 % methanol in distilled water) for 15 min at room temperature.

465   *SARS-CoV-2 strain MA10*

466   SARS-CoV-2 strain MA10 was titrated by plaque assay on VeroE6 cells obtained from Ralph Baric

467   (University of North Carolina at Chapel Hill) that stably express TMPRSS2 (VeroE6$_{UNC/TMPRSS2}$)

468   (referred to as VeroE6$_{UNC}$) in 6-well format. Briefly, $4x10^5$ cells were plated the day prior, medium

469   was aspirated and 500 µL of a serial 10-fold virus dilutions in Opti-MEM were added. Cells were

470   incubated for 90 min 37 °C and plates were moved every 20 min to prevent drying out of the

471   wells. The initial inoculum was removed, 2 mL overlay were added per well (DMEM containing

472   10 % FBS with 1.2 % microcrystalline cellulose (Avicel)). Cells were incubated for four days at 33

473   °C, followed by fixation with 7 % formaldehyde and crystal violet staining for 1 hour. The overlay

474   was removed, and virus was quantified by enumerating plaques. All SARS-CoV-2 MA10

475   experiments were performed in a biosafety level 3 laboratory. To verify SARS-CoV-2 MA10

476   identity and test for unwanted mutations, RNA from virus stocks was purified using TRIzol

477   Reagent (Thermo Fisher Scientific, #15596026). Briefly, 200 µL of each virus stock was added to

478   800 µL TRIzol Reagent, followed by 200 µL chloroform, which was then centrifuged at 12,000 G

479   for 5 min. The upper aqueous phase was moved to a new tube, mixed with an equal volume of

480   isopropanol, and then added to an RNeasy Mini Kit column (QIAGEN, #74014) to be further

481   purified following the manufacturer's instructions. Viral stocks were subsequently confirmed via

482   next generation sequencing using libraries for Illumina MiSeq.

483

484   <u>Intranasal treatments and infections</u>

485   For anesthesia, mice were intraperitoneally injected with a mixture of ketamine (80mg/kg;

486   Zoetis, #54771-2013-1) and xylazine (8.8 mg/kg; Akorn, #07-808-1947) in PBS. After mice were

487   sufficiently anesthetized, 30µL of inoculum was applied to one nostril. Mice were monitored until

488   they regained consciousness.

489   For infections, mice were inoculated with 6,000 PFU of SARS-CoV-2 MA10, 200 or 50 PFU of

490   influenza A/PR/8/34 virus for LD50 and sublethal infections, respectively.

491

492   <u>Isolation of bronchoalveolar lavage fluid</u>

493   Mice were euthanized and the trachea was carefully exposed. A 18G catheter equipped with a 3-

494   way cock stop valve was inserted into the trachea. Bronchoalveolar lavage fluid (BALF) was

495   obtained by flushing the airways with 5x 1mL of sterile PBS containing 2mM

496   ethylenediaminetetraacetic acid (EDTA). BALF was stored on ice at all times until further use.

497

498   <u>Alveolar macrophage culture</u>

499   Isolated BALF was counted, spun at 500 G for 5 minutes at 4 °C and resuspended in medium to

500   reach the desired cell concentration.

501   For short-term culture, cells were resuspended and cultured in RPMI medium (Thermo Fisher

502   Scientific #11875093) supplemented to contain 10% fetal bovine serum (FBS), 1% Penicillin-

503   Streptomycin (Thermo Fisher Scientific #15140122) and 1% L-Glutamine (Thermo Fisher Scientific

504   #A2916801). Cells were incubated over night, washed with PBS the next day and fresh medium

505   containing the respective stimuli was added.

506   Long-term culture of alveolar macrophages was carried out as previously described [25]. Briefly,

507   cells were resuspended and cultured in RPMI medium (Thermo Fisher Scientific #11875093)

508   supplemented to contain 10 % fetal bovine serum (FBS), 1 % Penicillin-Streptomycin (Thermo

509   Fisher Scientific #15140122), 1 % L-glutamine (Thermo Fisher Scientific #A2916801), 30 ng/mL

510   granulocyte-macrophage colony-stimulating factor (GM-CSF) (Peprotech #315-03), 10 ng/mL

511   transforming growth factor (TGF)-β1 (Peprotech #100-21), 1 μM Rosiglitazone (Sigma Aldrich

512   #R2408) and 50 μg/mL Gentamicin (Thermo Fisher Scientific #15750060). Cells were cultured in

513   standard tissue culture vessels, medium was changed every 3 days and split when they reached

514   70-80 % confluency. Typical alveolar macrophage cultures consist of adherent and suspended

515   cells. For splitting, culture supernatants were collected, cells were rinsed with Dulbecco's

516   phosphate buffered saline (PBS, Thermo Fisher Scientific #14190144). To detach adherent cells,

517   ESGRO Complete Accutase (Sigma Aldrich #SF006) was added and cells were incubated at 37 °C

518   for 5 to 10 minutes until cells were detached. Cells were completely detached and resuspended

519   in medium by pipetting. Cells were counted on a Countess automated cell counter (Invitrogen

520   #c10281), spun at 500 G for 5 minutes at 4 °C and resuspended in medium to reach the desired

521   cell concentration and plated into a new cell culture vessel.

522

523   *In vitro* polyIC treatment of alveolar macrophages

524   For all experiments, endotoxin-free polyinosinic-polycytidylic acid (polyIC, InvivoGen #tlrl-pic)

525   was used. Stimulation of alveolar macrophages with polyIC was done at 10 µg/mL for 24 hours

526   (establishment of innate immune memory) or 6 hours (acute response or recall response).

527   To establish innate immune memory in alveolar macrophages, cells were treated with 10 µg/mL

528   polyIC for 24 hours. Cells were washed with PBS (Thermo Fisher Scientific #14190144) and fresh

529   medium was added. 2 days after washing, fresh medium was added and/or cells were split if

530   necessary. 4 days after washing, cells were seeded into 24-well or 96-well plates. Cells were re-

531   stimulated the next day with polyIC for 6 hours (RT-qPCR, RNA-seq or immunofluorescence) or

532   24h (immunofluorescence).

533

534   VSV-GFP infection of alveolar macrophages

535   VSV-GFP infection of alveolar macrophages was carried out at a MOI of 0.01 PFU/cell. Medium

536   was aspirated from cell cultures and medium containing VSV-GFP at the desired dilution and 1

537   µg/mL Hoechst (Thermo Fisher Scientific #33342) was added. After 24 hours, medium was

538   aspirated and cells were fixed for 10 min in 4 % paraformaldehyde (Sigma Aldrich #F8775) at

539   room temperature, washed with 200 µL PBS (Thermo Fisher Scientific #14190144) and stored in

540   200 µL at 4 °C until imaging.

541

542   Alveolar macrophage transfer *in vivo*

543   Anesthetized mice were intranasally (i.n.) treated with 2x25 µL clodronate liposomes (Liposoma

544   #C-005) 3 days prior to alveolar macrophage transfer. Alveolar macrophages were isolated and

545   expanded *in vitro* as described above. Cells were treated with 10 µg/mL polyIC (InvivoGen #tlrl-

546   pic) or PBS (Thermo Fisher Scientific #14190144) and 1 day prior to transfer. At the day of

547   transfer, cells were detached and washed 2 times with 50 mL PBS and counted and concentration

548   was adjusted. Each mouse was i.n. transferred 700,000 cells in 30 µL PBS. Mice were allowed to

29

549 recover for 5 days and were subsequently challenged with 200 PFU (LD50) of influenza A virus

550 strain PR8 and body weight loss was monitored.

551

552 <u>RNA isolation</u>

553 Cells or tissue samples were collected in 1 mL TRIzol Reagent (Thermo Fisher Scientific

554 #15596026). Tissues were homogenized using glass beads (BioSpec Products #11079110) and a

555 MagNA Lyser (Roche Diagnostics) at 6,000 rpm and 30 seconds. Total RNA was isolated according

556 to the TRIzol/chloroform extraction protocol of the Ambion PureLink RNA Mini Kit (Thermo Fisher

557 Scientific #12183025). RNA concentration was determined on a NanoDrop Instrument (Thermo

558 Fisher Scientific) and RNA was stored at -80 °C.

559

560 <u>cDNA synthesis</u>

561 cDNA was synthetized using the RevertAid First Strand cDNA Synthesis Kit and random hexamer

562 primers (Thermo Fisher Scientific #K1622) according to the manufacturer's instructions.

563

564 <u>qPCR</u>

565 Quantitative PCRs (qPCR) were run and analyzed on a QuantStudio3 Real-Time PCR System

566 (Thermo Fisher Scientific) according to the PowerUP SYBR Green (Thermo Fisher Scientific

567 #25741) protocol with 1.5 to 15 ng cDNA input. Expression levels of *Eef1a* (5'-

568 GCAAAAACGACCCACCAATG-3', 5'-GGCCTGGATGGTTCAGGATA-3'), *Ifit1*

569 (5'TTACAGCAACCATGGGAGAGAATG-3', 5'-GGAACTGGACCTGCTCTGAGATTC-3'), *Ifitm3* (5'-

570 GCCTACTCCGTGAAGTCTAGGG-3', 5'-CCAAGGTGCTGATGTTCAGGC-3'), *Bst2* (5'-

571 TGTAGAGACGGGTTGCGAGC-3', 5'-CTCCTGAAGGGTCACCACGG-3'), *SARS-CoV-2 N* (5'-

572 TAATCAGACAAGGAACTGATTA-3', 5'-CGAAGGTGTGACTTCCATG-3') and *PR8 M* (5'-

573 CATGGAATGGCTAAAGACAAGACC-3', 5'-CCATTAAGGGCATTTTGGACA-3') were determined using

574 a standard qPCR protocol (step 1: 20 sec at 95 °C, step 2: 1 sec at 95 °C, step 3: 20 sec at 60 °C,

575 step 4: go to step 2 and repeat 40x, step 5: 1 sec at 95 °C, step 6: 20 sec at 60 °C, step 7: ramp

576 down up to 95 °C at +0.15 °C/s, step 8: 1 sec 95 °C, step 9: end).

577

578 Flow cytometry

579 Bronchoalveolar lavage fluid (BALF) was centrifuged at 500 G for 5 minutes at 4 °C. For bone

580 marrow (BM), red blood cells (RBC) were lysed by incubating cells with RBC Lysis Buffer

581 (Biolegend #420301) for 3 min at room temperature. To stop RBC lysis, 1 mL PBS (Thermo Fisher

582 Scientific #14190144) was added, and cells were centrifuged at 500 G for 5 minutes at 4 °C.

583 Supernatant was aspirated down to 100 µL, cells were resuspended and transferred to a V-

584 bottom 96-well plate. Plates were centrifuged at 500 G for 5 minutes at 4 °C. Supernatant was

585 aspirated and cells were resuspended in 25 µL FcR block per well (200x, Biolegend #101320)

586 diluted in FACS buffer (2 % FBS, 2 mM EDTA, 10g/L NaN_3) and incubated at room temperature

587 for 15 min. This step was omitted for BM samples. Next, 25 µL 2x surface staining mix diluted in

588 FACS buffer were added per well and cells were incubated for 30 min at 4 °C. For BM samples, 1x

589 surface staining mix diluted in FACS buffer was added. Cells were washed with 150 µL PBS per

590 well and resuspended in 100 µL viability dye. Cells were incubated for 15 min at room

591 temperature and washed twice with 100 µL FACS buffer per well before fixation with 4 %

592 paraformaldehyde (Sigma Aldrich #F8775) for 10 min at room temperature. Samples were

593 washed once with 200 µL FACS buffer and resuspended in 150-250 µL FACS buffer and stored at

594 4 °C until acquisition.

595 For BALF surface staining, anti-F4/80 (BV421, clone BM8, Biolegend #123137), anti-CD4 (BV510,

596 clone GK1.5, Biolegend #100449), anti-CD11c (BV605, clone N418, Biolegend #117333), anti-

597 CD11b (BV650, clone M1/70, Biolegend #101259), anti-CD69 (BV711, clone H1.2F3, Biolegend

598 #104537), anti-CD44 (FITC, clone IM7, Biolegend #103005), anti-SiglecF (PerCP-Cy5.5, clone

599 S17007L, Biolegend #155531), anti-CD3 (PE-Dazzle, clone 17A2, Biolegend #100245), anti-CD62L

600 (PE-Cy5, clone MEL-14, Biolegend #104410), anti-CD103 (PE-Cy7, clone QA17A24, Biolegend

601 #156905), anti-Ly6G (APC, clone 1A8, Biolegend #127613), anti-CD8a (AF647, clone 53-6.7,

602 Biolegend #100724), anti-CD45 (AF700, clone I3/2.3, Biolegend #147715), anti-NK1.1 (APC-Cy7,

603 clone S1701D, Biolegend #156509), anti-CD45.2 (APC, clone 104, Biolegend #109813), anti-

604 SiglecF (APC-Cy7, clone S17007L, Biolegend #155531), anti-CD11c (Pacific Blue, clone N418,

605 Biolegend #117321) were used.

31

606 For BM surface staining, Biotin anti-mouse Lineage Panel (Biolegend #133307), anti-CD150

607 (BV650, clone TC15-12F12.2, Biolegend #115932), anti-CD117 (BV785, clone 2B8, Biolegend

608 #105841), anti-CD48 (PerCP-Cy5.5, clone HM48-1, Biolegend #103421), anti-CD135 (PE, clone

609 A2F10, Biolegend #135305), anti-Sca1 (PE-Dazzle, clone E13-161.7, Biolegend #122527), anti-

610 CD16/32 (PE-Cy5, clone S17011E, Biolegend #156617), anti-CD34 (PE-Cy7, clone SA376A4,

611 Biolegend #152217), anti-CD127 (APC, clone S18006K, Biolegend #158205), anti-CD115 (APC-

612 Fire750, clone AFS98, Biolegend #135535), FITC Streptavidin (Biolegend #405201), BV421

613 Streptavidin (Biolegend #405226) were used.

614 For dead cell exclusion, Zombie Green Fixable Viability Kit (Biolegend #423111), Zombie Violet

615 Fixable Viability Kit (Biolegend #423114) and LIVE/DEAD Fixable Blue dead Cell Stain Kit (Thermo

616 Fisher Scientific #L23105) were used.

617

618 PKH26 labeling

619 Mice were anesthetized and intranasally treated with a 1:50 dilution of LumiTrace PKH26

620 (Lumiprobe #13201). 5 days after treatment, mice were intranasally challenged with virus.

621

622 Histological analyses

623 After euthanasia, murine lung tissues were excised and placed in 10 mL 10% neutral buffered

624 formalin (Fischer Scientific #SF100-4) for 48 hours. Samples were subsequently transferred to

625 70% ethanol for processing in a Leica ASP300 following a one hour, 13 step program. Samples

626 were embedded in paraffin using standard orientation procedures. Five-micron tissue sections

627 were collected onto Plus slides (Fisher Scientific #22-042-924), air-dried, and stored at room

628 temperature prior to use. Each sample was histochemically stained with hematoxylin-eosin.

629 Chromogenic immunohistochemistry (CIHC) was performed using unconjugated polyclonal

630 rabbit anti-SARS CoV-2 Nucleocapsid protein (GeneTex Cat# GTX135357, Lot# 43979, RRID:

631 AB_2868464). Lungs from SARS-CoV-2 recovered and naïve animals were sectioned on to the

632 same slide and used for antibody optimization. Initial optimization testing determined antigen

633 retrieval requirements at fixed concentration. Subsequent optimization manipulated

634 concentration and or incubation to establish final protocol parameters. Negative controls

635   consisted of primary antibody substituted with antibody diluent. All immunohistochemistry was

636   performed on a Ventana Medical Systems Discovery Ultra platform using Ventana's reagents and

637   detection kits unless otherwise noted. In brief, sections were deparaffinized online. Rabbit anti-

638   SARS-CoV-2 Nucleocapsid protein was diluted 1:200 (1.6 ug/ml) and incubated for 3 hours at

639   room temperature and with goat anti-rabbit horseradish peroxidase conjugated for 8 minutes

640   followed by DAB detection. Slides were washed in distilled water, counterstained with

641   hematoxylin, dehydrated through graded alcohols, cleared in xylene and mounted with synthetic

642   permanent media. Appropriate positive and negative controls were included with the study

643   sections.

644

645   Immunofluorescence

646   Immunofluorescence experiments were performed in black wall 96-well plates (Corning #3904).

647   At the respective time point, cells were fixed for 10 min in 4 % paraformaldehyde (Sigma Aldrich

648   #F8775) at room temperature and washed 2 times with 200 µL PBS (Thermo Fisher Scientific

649   #14190144). Next, cells were incubated with 100 µL ice cold methanol (Sigma Aldrich #34860)

650   for 10 min at -20 °C. After washing with 200 µL PBS, 50 µL of PBS containing 0.5% Triton X-100

651   (Sigma Aldrich #93443) was added for 5 minutes and then blocked with 50 µL 5% goat serum

652   (Jackson Immuno Research #005-000-121) in PBS for 30 min at room temperature. Primary

653   antibodies were added in 35 µL per well and incubated for 1 hour at room temperature. Cells

654   were washed 3 times with 200 µL PBS for 4 min before secondary antibodies and 1 µg/mL

655   Hoechst (Thermo Fisher Scientific #33342) were added in 35 µL per well and incubated for 1 hour

656   at room temperature. Afterwards, cells were washed 3 times with 200 µL PBS for 4 min and

657   stored in 200 µL PBS at 4 °C until imaging. Cells were imaged on a BioTek Cytation 7 or a Perkin

658   Elmer Operetta CLS instrument.

659

660   Image analyses

661   Images were analyzed and fluorescent intensities quantified using CellProfiler version 4.2.1 [54].

662   Subsequent analyses were performed using RStudio version 2023.03.0+386.

663

664 <u>Cytokine profiling</u>

665 Cytokines were quantified using Luminex xMAP technology for multiplexed quantification of 45

666 Mouse cytokines, chemokines and growth factors offered by Eve Technologies Corp. (Calgary,

667 Alberta, Canada). According to Eve Technologies, the multiplexing analysis was performed using

668 the Luminex™ 200 system (Luminex, Austin, TX, USA). Forty-five markers were simultaneously

669 measured in the samples using Eve Technologies' Mouse Cytokine 44-Plex Discovery Assay which

670 consists of two separate kits; one 32-plex and one 13-plex (Sigma, Burlington, Massachusetts,

671 USA). The assay was run according to the manufacturer's protocol. The 32-plex consisted of

672 Eotaxin, G-CSF, GM-CSF, IFNγ, IL-1α, IL-1β, IL-2, IL-3, IL-4, IL-5, IL-6, IL-7, IL-9, IL-10, IL-12(p40), IL-

673 12(p70), IL-13, IL-15, IL-17, IP-10, KC, LIF, LIX, MCP-1, M-CSF, MIG, MIP-1α, MIP-1β, MIP-2,

674 RANTES, TNFα, and VEGF. The 13-plex consisted of 6Ckine/Exodus2, Erythropoietin, Fractalkine,

675 IFNβ-1, IL-11, IL-16, IL-20, MCP-5, MDC, MIP-3α, MIP-3β, TARC, and TIMP-1. Assay sensitivities of

676 these markers range from 0.3 to 30.6 pg/mL for the 45-plex. Individual analyte sensitivity values

677 are available in the Sigma MILLIPLEX® MAP protocol.

678

679 <u>Bulk transcriptomics</u>

680 RNA was isolated as described above and were submitted to MedGenome Inc. (Foster City,

681 California, USA). Sequencing libraries were prepped using the Takara SMARTer Stranded Total

682 RNA-Seq Kit v3 or the Illumina TrueSeq RNA Library Prep Kit v2 and 150 bp paired-end sequencing

683 was performed on an Illumina NovaSeq instrument. Reads were aligned to the Mus musculus

684 genome mm10 GCRm38 (Fig 2) or GCRm39 (Fig 3) using STAR v. 2.7.10b. Read counts were

685 normalized, statistically analyzed and differentially expressed genes between conditions

686 identified using the DESeq2 package version 1.34.0 [55] in RStudio version 2023.03/0+386.

687

688 <u>Hierarchical clustering and gene ontology enrichment analyses</u>

689 For hierarchical clustering of bulk RNA transcriptomics, lowly expressed genes were excluded

690 (average FPKM across all conditions < 1) and only genes with an absolute log2 fold change greater

691 than 1 and an adjusted *p*-value lower than 0.05 were considered. Significantly regulated genes of

692 single cell RNA sequencing were identified using Seurat v4 [22]. Gene ontology (GO) enrichment

693 analyses for biological processes (BP) of identified genes of interest of gene clusters was

694 performed using the clusterProfiler package version 4.2.2 [56] and hierarchical clustering was

695 performed in in RStudio version 2023.03/0+386.

696

697 <u>Single cell RNA sequencing</u>

698 *Library preparation*

699 Bronchoalveolar lavage fluid was centrifuged at 500 G for 5 minutes at 4 °C and supernatant was

700 aspirated. Cells were resuspended in 300 µL PBS (Thermo Fisher Scientific #14190144), counted

701 and adjusted to equivalent concentrations. Cell suspensions were processed for scRNA-seq with

702 the 10x Chromium NextGEM Single-cell 3' v3.1 kit according to manufacturer's instructions. Each

703 sample (naïve/PR8 or SARS2/PR8) was loaded to an individual 10x Chromium controller Chip G

704 lane at a concentration for targeted recovery of 5,000 cells per lane. Barcode cDNA amplification

705 was performed with 12 cycles of PCR. Following Bioanalyzer QC, libraries were pooled and

706 sequenced on the Illumina NextSeq 500 instrument in paired end configuration (Read 1: 28 nt,

707 Read 2: 55 nt).

708 *Data processing*

709 Sequencing data was mapped and quantified to per cell gene expression counts using CellRanger

710 count (v5.0.0, 10x Genomics) with a mouse reference transcriptome (mm10) appended with

711 annotations for IAV PR8 and SARS-CoV-2 MA10 (joint reference prepared with CellRanger mkref).

712 Gene x cell matrices were further processed and analyzed with Seurat (v4.0.5) [57] in the R

713 statistical framework (v4.0.3). After exclusion of several mouse RNAs (*Gm42418*, *Gm26917*,

714 *AY036118*) associated with artifactual signals [58,59], quality thresholds were set based on data

715 exploration, and cells with fewer than 500 RNA UMI counts or greater than 10 % mitochondrial

716 RNA UMI counts were excluded from further analysis. Putative heterotypic doublets were

717 identified with scDblFinder (v1.4.0) [60] and excluded. Putative erythrocytes, defined as cells with

718 greater than 75% of RNA UMI counts composed of hemoglobin transcripts, were excluded.

719 *Data analysis*

720 SCtransform [61] (default parameters, with fraction of mitochondrial genes and Seurat cell cycle

721 score difference as regression factors) was used for normalization and variable feature selection.

722   Sample integration was performed with standard Seurat workflow; IAV PR8 genes (no SARS-CoV-

723   2 reads were detected in any sample) and variable immune receptor genes (i.e. T and B cell

724   receptor V, D, J genes) were excluded from integration and principal component dimensionality

725   reduction. For dimensionality reduction, the first 60 principal components of the integrated

726   dataset were used for UMAP generation, NearestNeighbor processing, and unsupervised graph-

727   based clustering.

728   "Major cell groups" were annotated with SingleR [62] (v1.4.1, cluster mode and single cell mode for

729   proliferating cells) and the Immunological Genome Project [63] reference datasets. Each major cell

730   group was extracted, re-clustered, and further annotated ("Subpopulation level", as in Figure 4)

731   based on canonical marker gene expression patterns.

732   ISG gene set [24] expression scores were calculated per cell from log1p-normalized RNA counts

733   using AddModuleScore() from Seurat v4.

734

735   <u>10X Multiome sequencing</u>

736   Bronchoalveolar lavage fluid from 3 animals per condition was pooled, centrifuged at 500 G for

737   5 minutes at 4 °C. The supernatant was aspirated, and dead cells were removed using the Dead

738   Cell Removal Kit (Miltenyi #130-090-101) and LS columns (Miltenyi #130-122-729) according to

739   manufacturer's instructions. Afterwards, nuclei were isolated according to the 10x Genomics

740   standard protocol (#CG000365 Rev C). Briefly, cells were centrifuged at 500 G for 5 minutes at 4

741   °C, supernatant was aspirated and 200 μL of lysis buffer (10 mM Tris-HCl, 10 mM NaCl, 3 mM

742   $MgCl_2$, 0.1 % Tween-20, 0.1 % IGEPAL CA630, 0.01 % digitonin, 1 % BSA, 1 mM DTT, 1 U/μL Sigma

743   Protector RNase inhibitor in nuclease free water) was added and mixed by pipetting. Cells were

744   incubated on ice for 3 min and 2 mL wash buffer (10 mM Tris-HCl, 10 mM NaCl, 3 mM $MgCl_2$, 0.1

745   % Tween-20, 1 % BSA, 1 mM DTT, 1 U/μL Sigma Protector RNase inhibitor in nuclease free water)

746   was added and mixed by inverting the tube. Samples were centrifuged at 500 G for 5 minutes at

747   4 °C, supernatant aspirated and nuclei washed two more times with 1 mL wash buffer. During

748   the last wash step, nuclei were filtered through a 40 μm FLowMi filter (Sigma Aldrich

749   #BAH136800040) into a new tube. After the last wash step, nuclei were resuspended in nuclei

36

750   buffer (10x Genomics #PN-20000153), counted using a Countess 3 cell counter (Thermo Fisher

751   Scientific #A49865) and concentration was adjusted to 3,000-5,000 nuclei/µL.

752   Nuclei were then processed using the Chromium Next GEM Single Cell Multiome ATAC + Gene

753   Expression Reagent Bundle (10x Genomics #1000285) and Chromium Controller & Next GEM

754   Accessory Kit (10x Genomics #1000202) following the manufacturer's user guide (10x Genomics

755   CG000338-Rev F). The single cell RNA and ATAC sequencing libraries were prepared using Dual

756   Index Kit TT Set A (10x Genomics #1000215) and Single Index Kit N Set A (10x Genomics

757   #1000212) respectively and sequenced on Illumina NovaSeq6000 platform.

758   *Data Preprocessing*

759   The Multiome data underwent preprocessing using the Cell Ranger ARC 1.0.0 pipeline and were

760   aligned to the mm10 genome. Subsequently, the Cell Ranger output was processed using the

761   Seurat Weighted Nearest Neighbor Pipeline. To eliminate low-quality cells, a filtering process was

762   employed as previously described [31]. Scrublet [64] was used on the RNAseq data to remove duplets.

763   From the pooled data, low-quality cells from individual samples were filtered out. For the RNA-

764   seq object, sctransform normalization was applied, followed by principal component analysis

765   (PCA). The top 30 principal components were used for UMAP embedding and clustering. This

766   process was repeated using 20 principal components.

767   Next, scATAC profiles from all samples were combined, and initial cell-type annotation was

768   performed based on scRNA-seq annotations. Peaks were called for each cell type using MACS2

769   (version 2.1.2). Redundant peaks were removed based on the q-value obtained from MACS2.

770   Using the resulting list of peak regions, the number of reads overlapping each peak window was

771   determined for each unique cell barcode tag. This generated a matrix of peak-by-cell counts

772   corresponding to ATAC reads within peaks for each cell profiled. High-quality cells were retained

773   based on having a fraction of reads in peaks (FRiP) greater than 0.4 and a sequencing depth of

774   more than 1000. The cells filtered out during this step were also removed from the scRNA object

775   to ensure consistency across both modalities.

776   After quality control, the scRNA-seq object was reprocessed using sctranform, PCA, clustering,

777   and UMAP embedding. Clusters were obtained from the scRNA-seq data using the default

778   parameters of Seurat (30 PCs for PCA). The annotations for these clusters were finalized based

779   on the expression of marker genes specific to distinct immune cell types. The same set of cells

780   was retained in the scATAC-seq component of the Multiome data, and the annotations were

781   transferred accordingly. The scATAC object was processed using the Signac pipeline, which

782   involved TF-IDF normalization, singular value decomposition (SVD), UMAP embedding, and

783   clustering.

784   *Motif Analysis*

785   To analyze motifs, position weight matrices (PWMs) from the JASPAR2020 database [65] and a

786   motif occurrence matrix using the mm10 genome were added to the separate assay. Per-cell TF

787   motif activity was calculated by employing the RunChromVAR function of Signac [66].

788   *Differential gene expression analysis*

789   For differential analysis of gene expression and TF activity, the FindMarker function of Seurat was

790   used. The Wilcoxon test was employed for statistical testing.

791

792   <u>Human data generation and analyses</u>

793   *Sample acquisition*

794   Study participants were enrolled at Weill Cornell Presbyterian Hospital during the initial infection

795   wave of SARS-CoV-2 in New York City (spring to winter 2020) and were most likely infected by

796   the original/non-variant strain of SARS-CoV-2. None of the patients had received a COVID-19

797   vaccine at time of blood collection. Peripheral blood mononuclear cells (PBMCs) and plasma was

798   isolated and single-cell Multiome datasets were generated as previously described [31].

799   The classification of subjects into groups was based on the COVID-19 World Health Organization

800   (WHO) Severity Classification. The groups included in this study were as follows: 1) healthy

801   volunteer donors, and 2) recovered mild COVID-19 patients (with a WHO severity score of 1-2).

802   To meet the inclusion criteria for each group, the following criteria were applied: 1) For healthy

803   volunteer donors, individuals had to be free of any clinical symptoms related to COVID-19 at the

804   time of blood collection. Negative SARS-CoV-2 PCR test results and/or seronegative status were

805   also considered when available. 2) For recovered mild COVID-19 patients, individuals had to have

806   a confirmed PCR test indicating SARS-CoV-2 infection, along with clinical symptoms of COVID-19

807   that did not require hospitalization. The prior infection status of both healthy volunteer donors

808   and recovered mild COVID-19 patients was confirmed through SARS-CoV-2 serological testing

809   after blood donation. Blood samples were collected using EDTA or sodium heparin-coated

810   vacutainers and were kept on gentle agitation until processing. All blood samples were processed

811   on the same day as collection. Information regarding age, sex, and comorbidities was obtained

812   either through EPIC EHR records or, if not available, through a standardized form filled out at the

813   time of donation.

814

815

816   **References**

817   1.   Randolph, H. E. & Barreiro, L. B. Herd Immunity: Understanding COVID-19. *Immunity* **52**,

818   737–741 (2020).

819   2.   Naik, S. & Fuchs, E. Inflammatory memory and tissue adaptation in sickness and in

820   health. *Nature* **607**, 249–255 (2022).

821   3.   Foster, S. L., Hargreaves, D. C. & Medzhitov, R. Gene-specific control of inflammation by

822   TLR-induced chromatin modifications. *Nature* **447**, 972–978 (2007).

823   4.   Netea, M. G. *et al.* Defining trained immunity and its role in health and disease. *Nat. Rev.*

824   *Immunol.* (2020) doi:10.1038/s41577-020-0285-6.

825   5.   Naik, S. *et al.* Inflammatory memory sensitizes skin epithelial stem cells to tissue damage.

826   *Nature* **550**, 475–480 (2017).

827   6.   Kaufmann, E. *et al.* BCG Educates Hematopoietic Stem Cells to Generate Protective

828   Innate Immunity against Tuberculosis. *Cell* **172**, 176-190.e19 (2018).

829   7.   de Laval, B. *et al.* C/EBPβ-Dependent Epigenetic Memory Induces Trained Immunity in

830   Hematopoietic Stem Cells. *Cell Stem Cell* **26**, 657-674.e8 (2020).

831   8.   Yao, Y. *et al.* Induction of Autonomous Memory Alveolar Macrophages Requires T Cell

832   Help and Is Critical to Trained Immunity. *Cell* **175**, 1634-1650.e17 (2018).

833   9.   Kleinnijenhuis, J. *et al.* Long-lasting effects of BCG vaccination on both heterologous

834   Th1/Th17 responses and innate trained immunity. *J. Innate Immun.* **6**, 152–8 (2014).

835 10. Cirovic, B. *et al.* BCG Vaccination in Humans Elicits Trained Immunity via the

836   Hematopoietic Progenitor Compartment. *Cell Host Microbe* **28**, 322-334.e5 (2020).

837 11. Moorlag, S. J. C. F. M. *et al.* BCG Vaccination Induces Long-Term Functional

838   Reprogramming of Human Neutrophils. *Cell Rep.* **33**, 108387 (2020).

839 12. Garly, M. L. *et al.* BCG scar and positive tuberculin reaction associated with reduced child

840   mortality in West Africa: A non-specific beneficial effect of BCG? *Vaccine* **21**, 2782–2790

841   (2003).

842 13. Zhou, P. *et al.* A pneumonia outbreak associated with a new coronavirus of probable bat

843   origin. *Nature* **579**, 270–273 (2020).

844 14. Carabelli, A. M. *et al.* SARS-CoV-2 variant biology: immune escape, transmission and

845   fitness. *Nat. Rev. Microbiol.* **21**, 162–177 (2023).

846 15. Aegerter, H., Lambrecht, B. N. & Jakubzick, C. V. Biology of lung macrophages in health

847   and disease. *Immunity* **55**, 1564–1580 (2022).

848 16. Hashimoto, D. *et al.* Tissue-resident macrophages self-maintain locally throughout adult

849   life with minimal contribution from circulating monocytes. *Immunity* **38**, 792–804 (2013).

850 17. Zhu, B. *et al.* Uncoupling of macrophage inflammation from self-renewal modulates host

851   recovery from respiratory viral infection. *Immunity* **54**, 1200-1218.e9 (2021).

852 18. Zahalka, S. *et al.* Trained immunity of alveolar macrophages requires metabolic rewiring

853   and type 1 interferon signaling. *Mucosal Immunol.* **15**, 896–907 (2022).

854 19. Wang, T. *et al.* Influenza-trained mucosal-resident alveolar macrophages confer long-

855   term antitumor immunity in the lungs. *Nat. Immunol.* **24**, 423–438 (2023).

856 20. Leist, S. R. *et al.* A Mouse-Adapted SARS-CoV-2 Induces Acute Lung Injury and Mortality

857   in Standard Laboratory Mice. *Cell* **183**, 1070-1085.e12 (2020).

858 21. Dinnon, K. H. *et al.* SARS-CoV-2 infection produces chronic pulmonary epithelial and

859   immune cell dysfunction with fibrosis in mice. *Sci. Transl. Med.* **14**, (2022).

860 22. Hao, Y. *et al.* Integrated analysis of multimodal single-cell data. *Cell* **184**, 3573-3587.e29

861   (2021).

862 23. Schep, A. N., Wu, B., Buenrostro, J. D. & Greenleaf, W. J. chromVAR: inferring

863   transcription-factor-associated accessibility from single-cell epigenomic data. *Nat.*

864   *Methods* **14**, 975–978 (2017).

865 24. Schoggins, J. W. *et al.* A diverse range of gene products are effectors of the type i

866   interferon antiviral response. *Nature* **472**, 481–485 (2011).

867 25. Gorki, A.-D. *et al.* Murine Ex Vivo Cultured Alveolar Macrophages Provide a Novel Tool to

868   Study Tissue-Resident Macrophage Behavior and Function. *Am. J. Respir. Cell Mol. Biol.*

869   **66**, 64–75 (2022).

870 26. Brandes, M., Klauschen, F., Kuchen, S. & Germain, R. N. A systems analysis identifies a

871   feedforward inflammatory circuit leading to lethal influenza infection. *Cell* **154**, 197–212

872   (2013).

873 27. Mitroulis, I. *et al.* Modulation of Myelopoiesis Progenitors Is an Integral Component of

874   Trained Immunity. *Cell* **172**, 147-161.e12 (2018).

875 28. Kaufmann, E. *et al.* BCG vaccination provides protection against IAV but not SARS-CoV-2.

876   *Cell Rep.* **38**, 110502 (2022).

877 29. Khan, N. *et al.* M. tuberculosis Reprograms Hematopoietic Stem Cells to Limit

878   Myelopoiesis and Impair Trained Immunity. *Cell* **183**, 752-770.e22 (2020).

879 30. Larsen, S. B. *et al.* Establishment, maintenance, and recall of inflammatory memory. *Cell*

880   *Stem Cell* 1–17 (2021) doi:10.1016/j.stem.2021.07.001.

881 31. Cheong, J.-G. *et al.* Epigenetic Memory of COVID-19 in Innate Immune Cells and Their

882   Progenitors. *bioRxiv* 2022.02.09.479588 (2022) doi:10.1101/2022.02.09.479588.

883 32. Murphy, J., Summer, R., Wilson, A. A., Kotton, D. N. & Fine, A. The prolonged life-span of

884   alveolar macrophages. *Am. J. Respir. Cell Mol. Biol.* **38**, 380–5 (2008).

885 33. Misharin, A. V *et al.* Monocyte-derived alveolar macrophages drive lung fibrosis and

886   persist in the lung over the life span. *J. Exp. Med.* **214**, 2387–2404 (2017).

887 34. Aegerter, H. *et al.* Influenza-induced monocyte-derived alveolar macrophages confer

888   prolonged antibacterial protection. *Nat. Immunol.* **21**, 145–157 (2020).

889 35. Li, F. *et al.* Monocyte-derived alveolar macrophages autonomously determine severe

890   outcome of respiratory viral infection. *Sci. Immunol.* **7**, (2022).

891 36. Wimmers, F. *et al.* The single-cell epigenomic and transcriptional landscape of immunity

892   to influenza vaccination. *Cell* 1–21 (2021) doi:10.1016/j.cell.2021.05.039.

893   37.   Rodríguez-Prados, J.-C. *et al.* Substrate fate in activated macrophages: a comparison

894   between innate, classic, and alternative activation. *J. Immunol.* **185**, 605–14 (2010).

895   38.   Jha, A. K. *et al.* Network integration of parallel metabolic and transcriptional data reveals

896   metabolic modules that regulate macrophage polarization. *Immunity* **42**, 419–430

897   (2015).

898   39.   Lercher, A., Baazim, H. & Bergthaler, A. Systemic Immunometabolism: Challenges and

899   Opportunities. *Immunity* **53**, 496–509 (2020).

900   40.   Gu, H. *et al.* Vaccination induces rapid protection against bacterial pneumonia via

901   training alveolar macrophage in mice. *Elife* **10**, (2021).

902   41.   Kamada, R. *et al.* Interferon stimulation creates chromatin marks and establishes

903   transcriptional memory. *Proc. Natl. Acad. Sci. U. S. A.* **115**, E9162–E9171 (2018).

904   42.   Pulendran, B. & Ahmed, R. Translating innate immunity into immunological memory:

905   implications for vaccine development. *Cell* **124**, 849–63 (2006).

906   43.   Ifrim, D. C. *et al.* Trained immunity or tolerance: Opposing functional programs induced

907   in human monocytes after engagement of various pattern recognition receptors. *Clin.*

908   *Vaccine Immunol.* **21**, 534–545 (2014).

909   44.   Novakovic, B. *et al.* β-Glucan Reverses the Epigenetic State of LPS-Induced Immunological

910   Tolerance. *Cell* **167**, 1354-1368.e14 (2016).

911   45.   Roquilly, A. *et al.* Author Correction: Alveolar macrophages are epigenetically altered

912   after inflammation, leading to long-term lung immunoparalysis. *Nat. Immunol.* **21**, 962–

913   962 (2020).

914   46.   Jurado-Camino, T. *et al.* Chronic lymphocytic leukemia: a paradigm of innate immune

915   cross-tolerance. *J. Immunol.* **194**, 719–27 (2015).

916   47.   Jeljeli, M. *et al.* Trained immunity modulates inflammation-induced fibrosis. *Nat.*

917   *Commun.* **10**, 5670 (2019).

918   48.   Ordovas-Montanes, J. *et al.* Allergic inflammatory memory in human respiratory

919   epithelial progenitor cells. *Nature* **560**, 649–654 (2018).

920   49.   Lechner, A. *et al.* Macrophages acquire a TNF-dependent inflammatory memory in

921   allergic asthma. *J. Allergy Clin. Immunol.* **149**, 2078–2090 (2022).

922   50.   Li, X. *et al.* Maladaptive innate immune training of myelopoiesis links inflammatory

923   comorbidities. *Cell* **185**, 1709-1727.e18 (2022).

924   51.   Kimura, T. *et al.* Essential and non-redundant roles of p48 (ISGF3 gamma) and IRF-1 in

925   both type I and type II interferon responses, as revealed by gene targeting studies. *Genes*

926   *Cells* **1**, 115–24 (1996).

927   52.   Blight, K. J., McKeating, J. A. & Rice, C. M. Highly permissive cell lines for subgenomic and

928   genomic hepatitis C virus RNA replication. *J. Virol.* **76**, 13001–14 (2002).

929   53.   Dalton, K. P. & Rose, J. K. Vesicular stomatitis virus glycoprotein containing the entire

930   green fluorescent protein on its cytoplasmic domain is incorporated efficiently into virus

931   particles. *Virology* **279**, 414–21 (2001).

932   54.   Stirling, D. R. *et al.* CellProfiler 4: improvements in speed, utility and usability. *BMC*

933   *Bioinformatics* **22**, 433 (2021).

934   55.   Love, M. I., Huber, W. & Anders, S. Moderated estimation of fold change and dispersion

935   for RNA-seq data with DESeq2. *Genome Biol.* **15**, 550 (2014).

936   56.   Wu, T. *et al.* clusterProfiler 4.0: A universal enrichment tool for interpreting omics data.

937   *Innov.* **2**, 100141 (2021).

938   57.   Stuart, T. *et al.* Comprehensive Integration of Single-Cell Data. *Cell* **177**, 1888-1902.e21

939   (2019).

940   58.   Liu, Y. *et al.* Single-Cell Profiling Reveals Divergent, Globally Patterned Immune

941   Responses in Murine Skin Inflammation. *iScience* **23**, 101582 (2020).

942   59.   Kimmel, J. C. *et al.* Murine single-cell RNA-seq reveals cell-identity- and tissue-specific

943   trajectories of aging. *Genome Res.* **29**, 2088–2103 (2019).

944   60.   Germain, P.-L., Lun, A., Garcia Meixide, C., Macnair, W. & Robinson, M. D. Doublet

945   identification in single-cell sequencing data using scDblFinder. *F1000Research* **10**, 979

946   (2021).

947   61.   Hafemeister, C. & Satija, R. Normalization and variance stabilization of single-cell RNA-

948   seq data using regularized negative binomial regression. *Genome Biol.* **20**, 296 (2019).

949   62.   Aran, D. *et al.* Reference-based analysis of lung single-cell sequencing reveals a

950   transitional profibrotic macrophage. *Nat. Immunol.* **20**, 163–172 (2019).

951   63.   Heng, T. S. P., Painter, M. W. & Immunological Genome Project Consortium. The

952   Immunological Genome Project: networks of gene expression in immune cells. *Nat.*

953   *Immunol.* **9**, 1091–4 (2008).

954   64.   Wolock, S. L., Lopez, R. & Klein, A. M. Scrublet: Computational Identification of Cell

955   Doublets in Single-Cell Transcriptomic Data. *Cell Syst.* **8**, 281-291.e9 (2019).

956   65.   Fornes, O. *et al.* JASPAR 2020: update of the open-access database of transcription factor

957   binding profiles. *Nucleic Acids Res.* **48**, D87–D92 (2020).

958   66.   Stuart, T., Srivastava, A., Madad, S., Lareau, C. A. & Satija, R. Single-cell chromatin state

959   analysis with Signac. *Nat. Methods* **18**, 1333–1341 (2021).

960

961

Figure 1

Figure 1: Past SARS-CoV-2 infection establishes epigenetic memory in airway-resident macrophages.
(A) Body weights of naïve and SARS-CoV-2 (strain MA10) infected C57Bl/6J mice. n = 11-12. (B) UMAP clustering of single nuclei combined ATAC/RNA-seq data (10x Multiome) and annotated cell clusters of airway-resident cells from naïve and SARS-CoV-2-recovered mice based on ATAC-seq data. n = 3. (C) Recovered and naïve sample annotation of UMAP clustering (B) with dashed line indicating the macrophage subset. (D) TF motif-associated chromatin accessibility analyses of recovered vs. naïve sub-setted macrophages. (E) Quantification of mean fluorescent intensity of nuclear IRF3 in airway-resident macrophages isolated from naïve and SARS-CoV-2-recovered animals and representative image. n = 3. Data are mean ± s.e.m. n values indicate the number of mice or replicates. For (D), statistical analysis was performed using Wilcoxon's test. For (E), statistical analysis was performed using Student's t-test with Bonferroni correction when multiple comparisons were performed. *p < 0.05; **p < 0.01; ***p < 0.001.

Figure S1

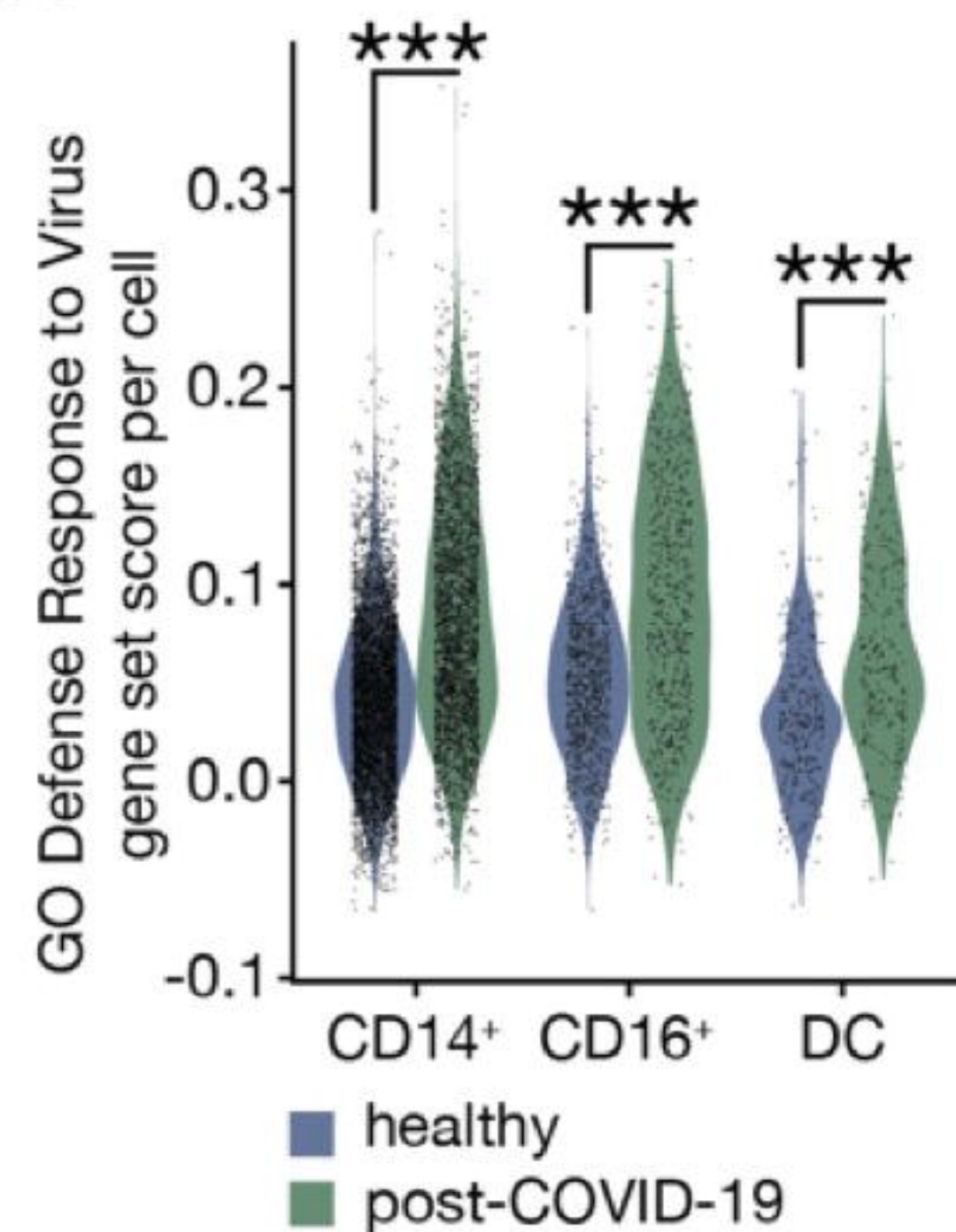**Figure S1: Characterization of naïve and SARS-CoV-2-recovered animals**

(A) RT-qPCR analyses of SARS-CoV-2 N transcript levels in lung tissue of naïve, SARS-CoV-2-recovered or acutely infected (6 days post infection with SARS-CoV-2 strain B.1.351) C57Bl/6J mice. n = 2-5. (B) Histological analyses of naïve, SARS-CoV-2-recovered and acutely infected (3 days post infection with SARS-CoV-2 strain MA10). n = 5. (C) RT-qPCR analyses of Ifit1, Bst2, Ifitm3, Isg15, Tnfa and Il-6 transcript levels in lung tissue of naïve and SARS-CoV-2-recovered animals. n = 3-4. (D) Flow cytometric analyses of alveolar macrophages (CD45+CD11c+SiglecF+), NK cells (CD45+NK1.1+) and neutrophils (CD45+CD11b+Ly6G+) in bronchoalveolar lavage fluid (BALF) of naïve and SARS-CoV-2-recovered animals. n = 7-8. (E-F) Cytokine profiling of BALF isolated from recovered and naïve animals. n = 5. (G) Flow cytometric analyses of abundance of hematopoietic progenitor cells (long-term hematopoietic stem cells (LT-HSC), short-term hematopoietic stem cells (ST-HSC), common lymphoid progenitor cells (CLP), multipotent hematopoietic progenitor cells (MPP), granulocyte-monocyte progenitor cells (GMP), common myeloid progenitor cells (CMP), megakaryocyte/erythroid progenitor cells (MEP)) in the bone marrow of naïve and SARS-CoV-2-recovered animals. n = 5. (H) Flow cytometric analyses of T cell subsets in BALF of naïve and SARS-CoV-2-recovered animals. n = 5. (I) UMAP clustering of the macrophage subset from single nuclei combined ATAC/RNA-sequencing data obtained from BALF of naïve and SARS-CoV-2-recovered animals. n = 5. (J) Top 10 enriched gene ontology (GO) terms analyses of significantly regulated genes of recovered vs. naïve macrophages (I). (K) Differentially expressed genes (DEG, absolute log2 fold change > 0.5) in macrophages (I) of recovered and naïve animals. Top 10 significant DEG by fold change are labelled. (L) Quantification of mean fluorescent intensity of nuclear RELA (p65) in airway-resident macrophages isolated from naïve and SARS-CoV-2-recovered animals. n = 3. Data are mean ± s.e.m. n values indicate the number of mice or replicates. For (A, C-H and L), statistics were calculated using Student's t-test with Bonferroni correction when multiple comparisons were performed. For (K), statistical analysis was performed using Wilcoxon rank sum test with Bonferroni correction. For (J), hypergeometric p values were adjusted for multiple testing with Benjamini-Hochberg correction. *p < 0.05; **p < 0.01; ***p < 0.001.
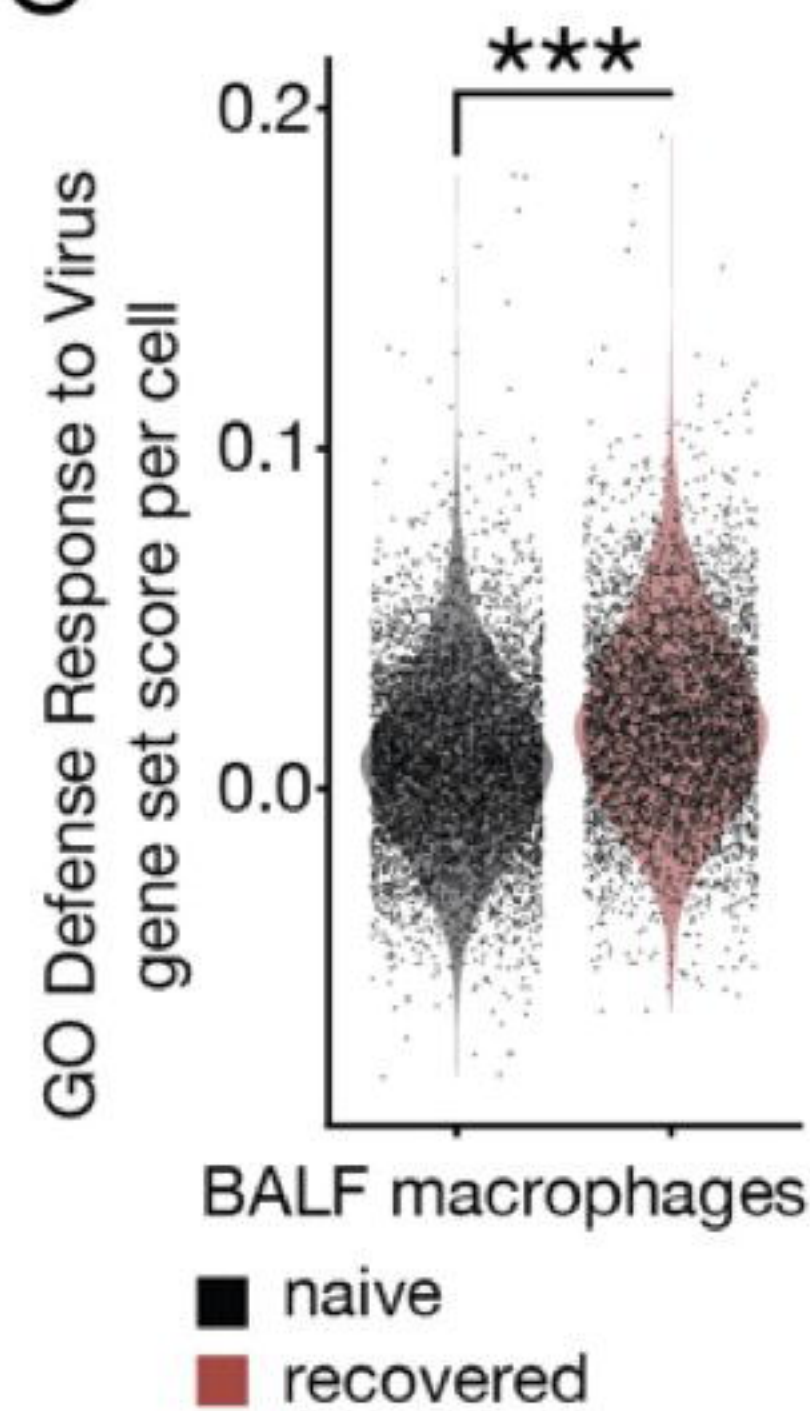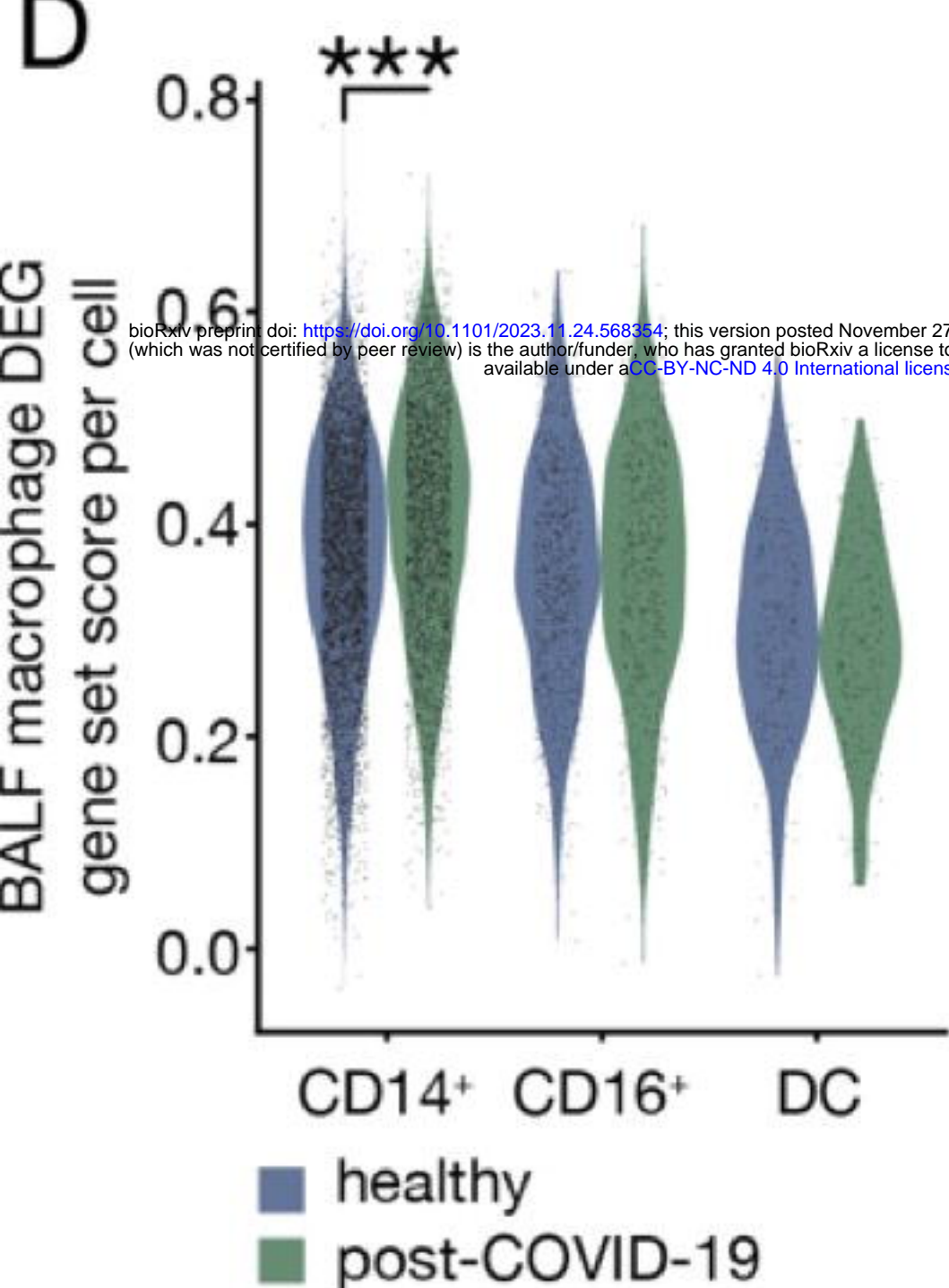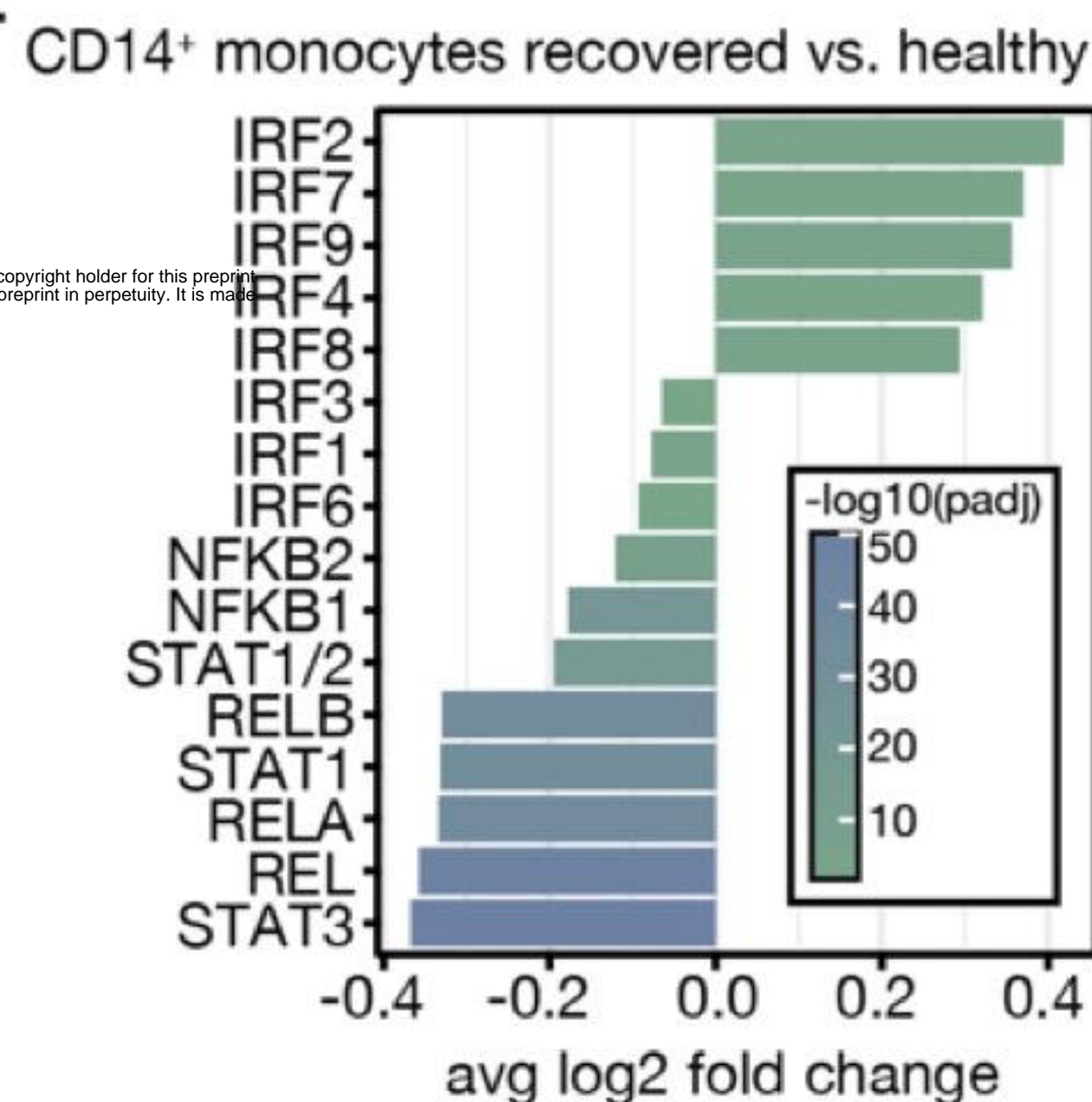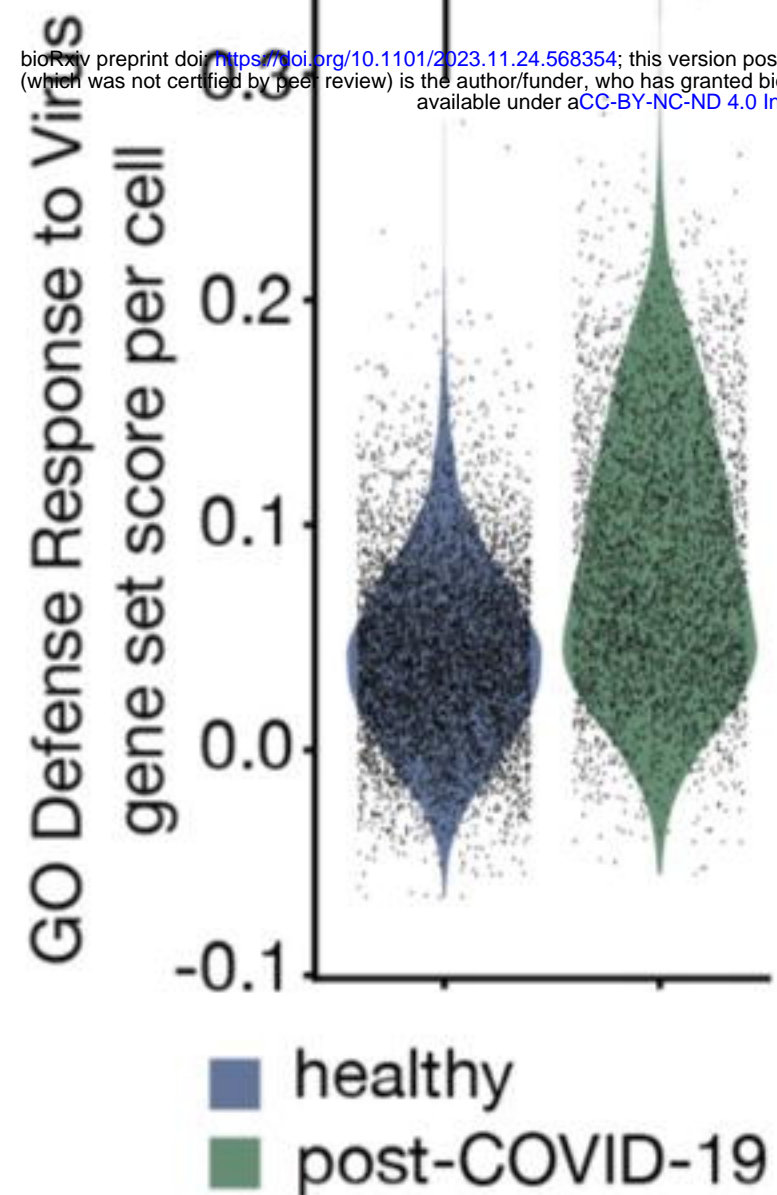
Figure 2

Figure 2: Past COVID-19 establishes epigenetic memory in circulating monocytes in patients.
(A) UMAP clustering of single nuclei combined ATAC/RNA-seq data and annotated cell clusters of peripheral blood mononu-clear cells (PBMCs) of recovered (2-4 months) mild COVID-19 and healthy patients with dashed line indicating the myeloid cell subset. n = 3-7. (B-C) Gene set expression score of GO: Defense Response to Virus in recovered and healthy circulating human myeloid cells (CD14+ and CD16+ monocytes and dendritic cells) (B) and murine BALF macrophages (C). (D) Gene set expression score of differentially expressed gene (DEG) module in circulating human myeloid cells. (E) Significantly different accessible TF motif-associated chromatin of recovered vs. healthy CD14+ monocytes. Data are represented as violin plots with each dot corresponding to one individual cell. For (B-E), statistical analyses were performed using Wilcoxon's test. *p < 0.05; **p < 0.01; ***p < 0.001.
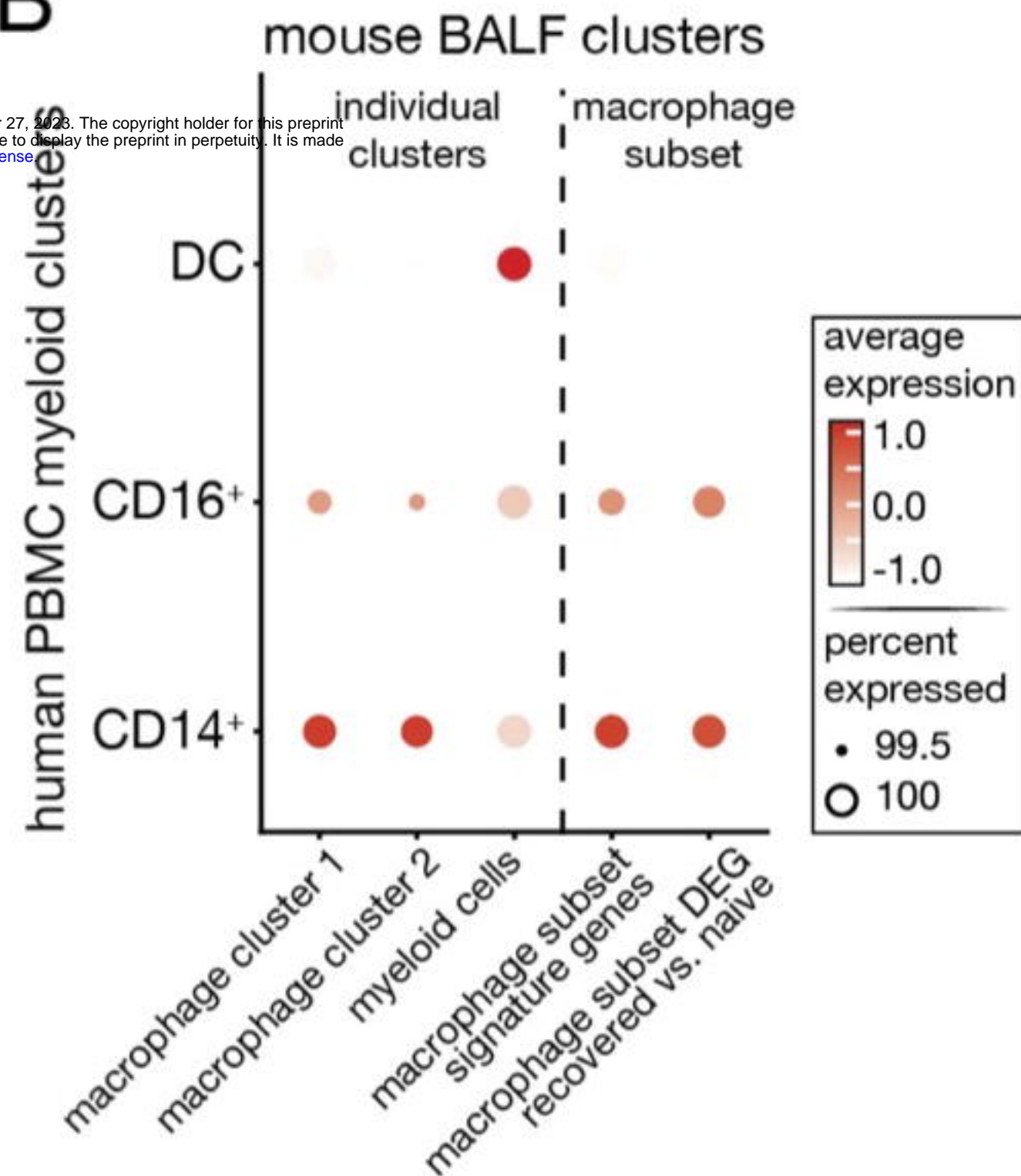
Figure S2

Figure S2: Characterization of naïve and SARS-CoV-2-recovered patient PBMCs

(A) Gene set expression score of GO: Defense Response to Virus across all recovered and healthy circulating human myeloid cells. (B) Expression of BALF cluster signature genes and macrophage subset (Figure 1I) differentially expressed gene (DEG) modules in circulating human myeloid cells (CD14+ and CD16+ monocytes and dendritic cells). Data are represented as violin plots or dotplot with each dot corresponding to one individual cell or cell cluster, respectively. For (A-B), statistical analysis was performed using Wilcoxon rank sum test with Bonferroni correction. *p < 0.05; **p < 0.01; ***p < 0.001.
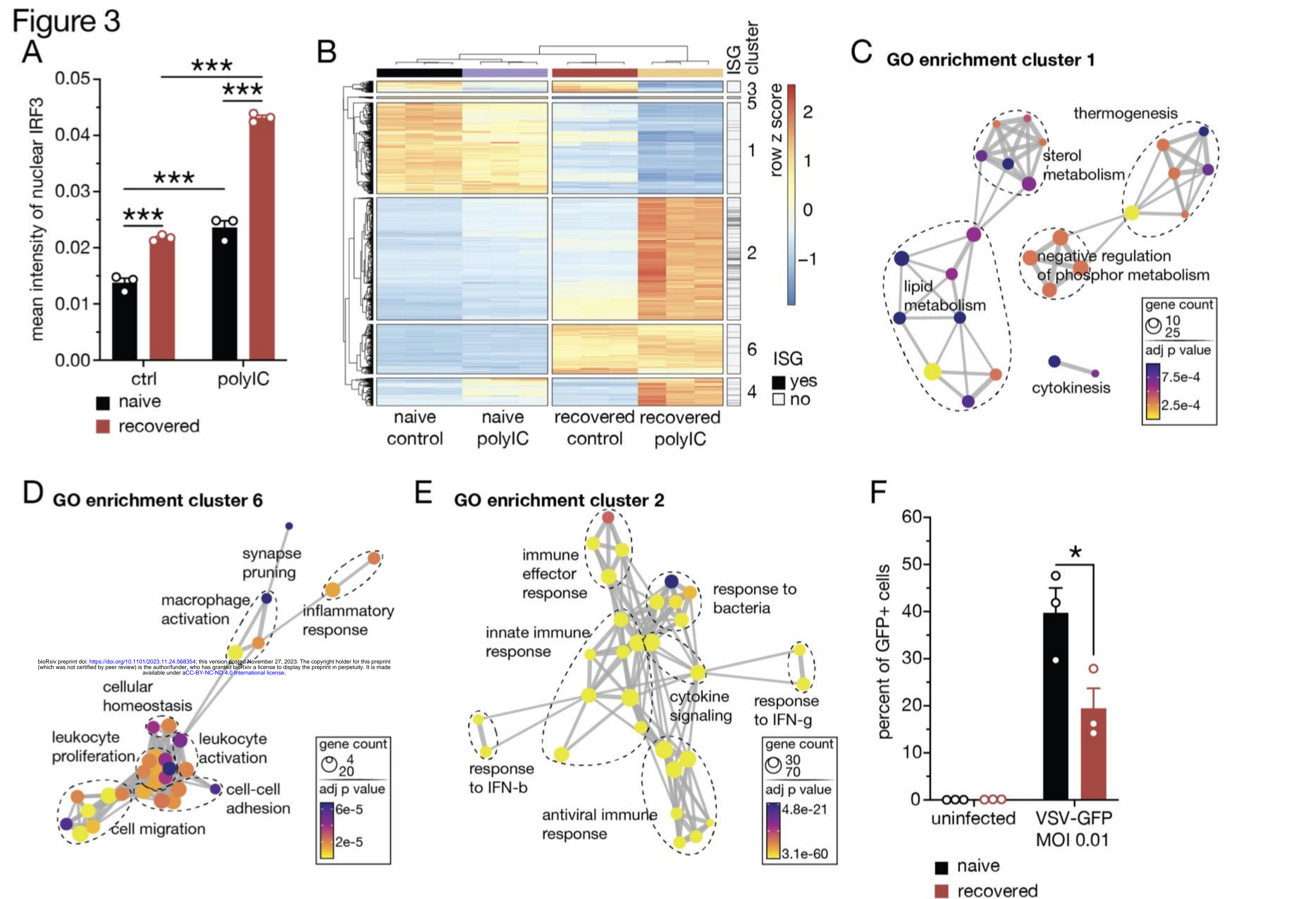
Figure 3: Past SARS-CoV-2 infection leads to increased secondary antiviral responses in airway-resident macrophages.

(A) Quantification of mean fluorescent intensity (MFI) of IRF3 in control– or polyIC-stimulated airway-resident macrophages isolated from naïve and SARS-CoV-2-recovered animals after 24 hours. n = 3. (B) Hierarchical clustering of differentially expressed genes (DEG) of control– or polyIC-stimulated airway-resident macrophages isolated from naïve or SARS-CoV-2-recovered animals after 6 hours. n = 3. (C-E), Gene ontology (GO) enrichment analyses of genes in clusters 1 (C), 6 (D), 2 (E). (F) Percent of VSV-GFP infected airway-resident macrophages isolated from naïve or SARS-CoV-2-recovered animals. n = 3. For (A and F), statistics were calculated using Student's t-test with Bonferroni correction when multiple comparisons were performed. For (C-E), hypergeometric p values were adjusted for multiple testing with Benjamini-Hochberg correction. *p < 0.05; **p < 0.01; ***p < 0.001.

Figure S3

- ● naive
- ● recovered
- ● naive + polyIC
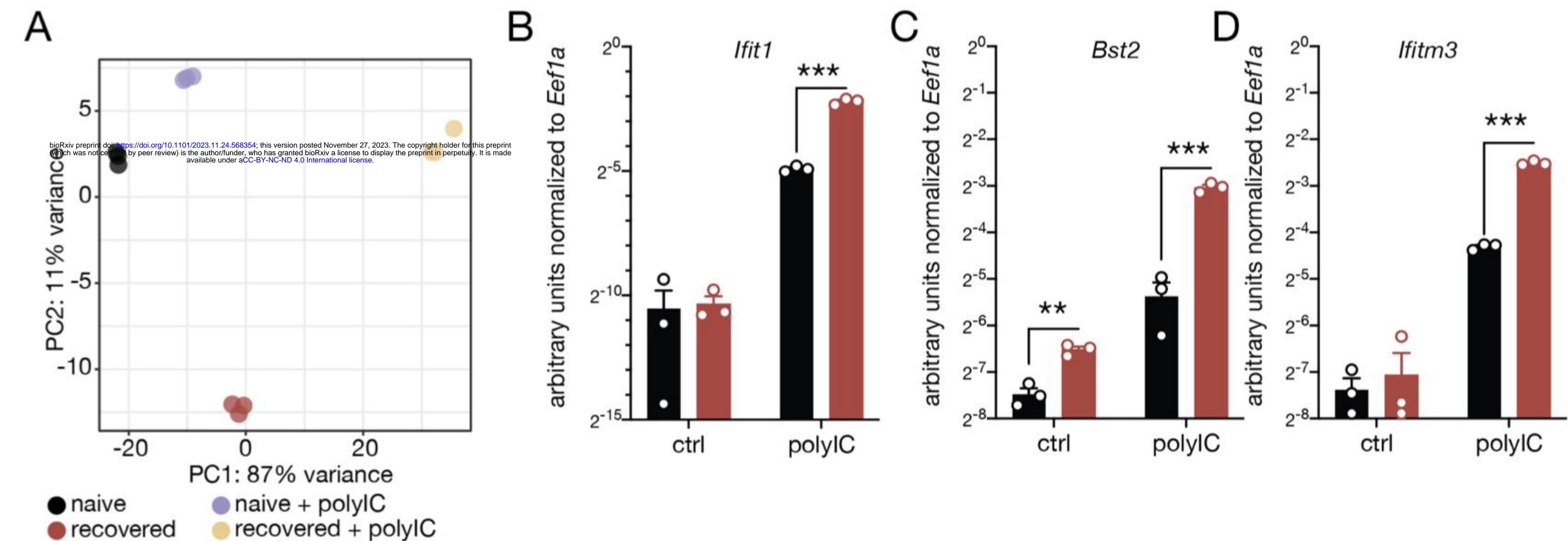- ● recovered + polyIC

Figure S3: Characterization of secondary response of airway-resident macrophages isolated from naïve and SARS-CoV-2-recovered animals

(A) Principal component analyses of transcriptomic profile of control– or polyIC-stimulated airway-resident macrophages isolated from naïve or SARS-CoV-2-recovered animals. n = 3. (B-D), RT-qPCR analyses of Ifit1 (B), Ifitm3 (C) and Bst2 (D) transcript levels in control– or polyIC-stimulated airway-resident macrophages isolated from naïve or SARS-CoV-2-recovered animals. n = 3. Data are mean ± s.e.m. n values indicate the number of mice or replicates. For (B-D), statistics were calculated using Student's t-test with Bonferroni correction when multiple comparisons were performed. *p < 0.05; **p < 0.01; ***p < 0.001.
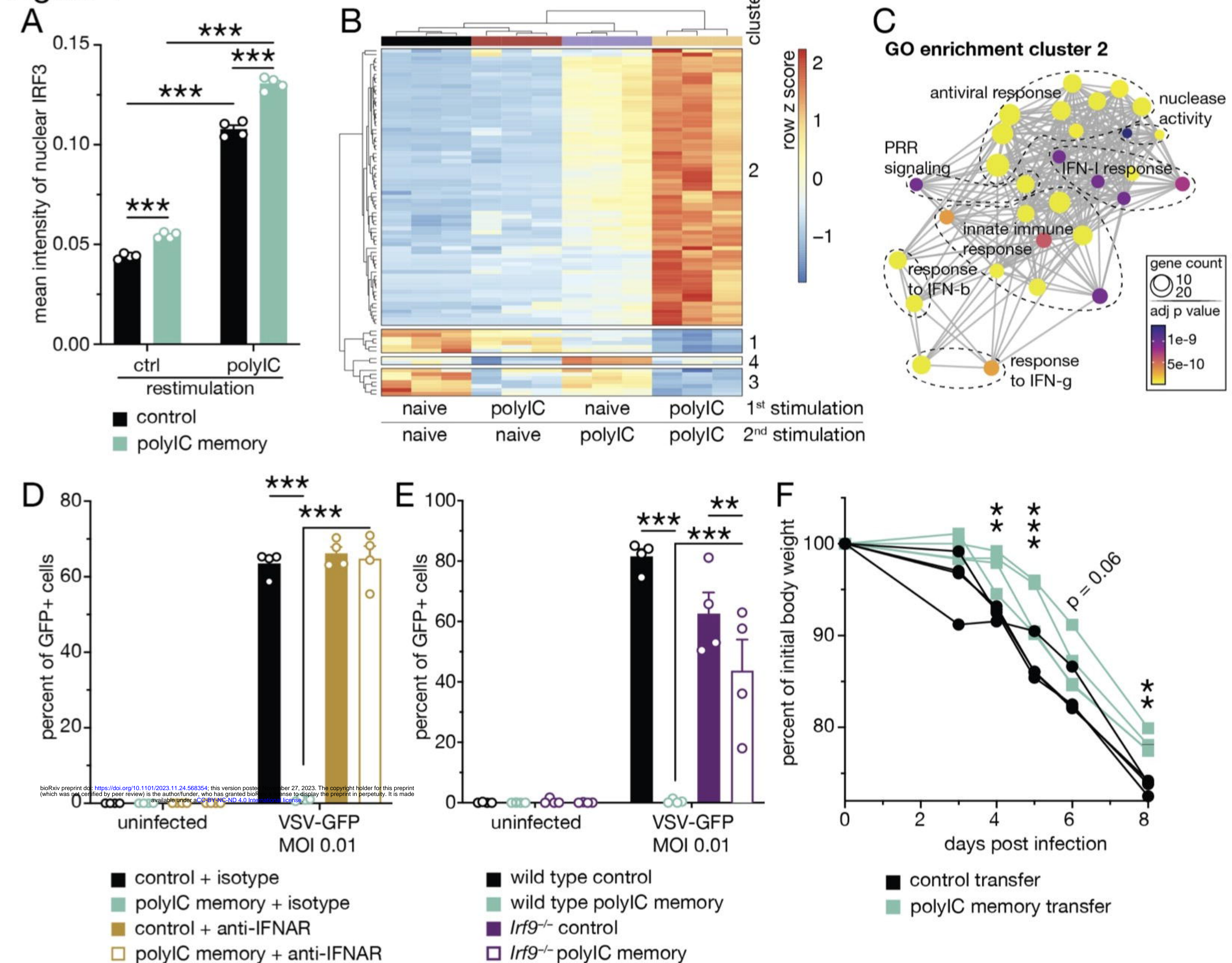
Figure 4

Figure 4: Viral PAMP exposure is sufficient to establish innate immune memory in alveolar macrophages in vitro.
(A) Quantification of mean fluorescent intensity (MFI) of IRF3 in control– or polyIC-stimulated control– or polyIC-experienced in vitro cultured alveolar macrophages after 24 hours. n = 4. (B) Hierarchical clustering of differentially expressed genes (DEG) of polyIC/polyIC vs. control/polyIC alveolar macrophages 6 hours after re-stimulation. n = 3. (C) Gene ontology (GO) enrichment analyses of genes in clusters 2. (D) Percent of VSV-GFP infected control– or polyIC-experienced alveolar macrophages with or without anti-IFNAR blocking antibody treatment during initial polyIC exposure. n = 4. (E) Percent of VSV-GFP infected control– or polyIC-experienced wild type or Irf9–/– alveolar macrophages. n = 4. (F) Body weights of influenza A/PR/8/34 virus infected C57Bl/6J mice following transfer of control– or polyIC-experienced alveolar macrophages. n = 4. Data are mean ± s.e.m. n values indicate the number of mice or replicates. For (A), statistics were calculated using Student's t-test with Bonferroni correction when multiple comparisons were performed. For (C), hypergeometric p values were adjusted for multiple testing with Benjamini-Hochberg correction. For (D-E), statistical analysis was performed using Two-Way ANOVA comparison with Bonferroni correction. For (F), statistical analysis was performed using Two-Way ANOVA comparison with Bonferroni correction. *p < 0.05; **p < 0.01; ***p < 0.001.

Figure S4

Figure S4: Characterization of secondary response of polyIC-experienced alveolar macrophages in vitro

(A) Quantification of mean fluorescent intensity of RELA (p65) in control– or polyIC-stimulated control– or polyIC-experienced in vitro cultured alveolar macrophages after 6 hours. n = 4. (B-D), RT-qPCR of Ifit1 (B), Ifitm3 (C) and Bst2 (D) transcript levels of polyIC/polyIC vs. control/polyIC stimulated in vitro cultured alveolar macrophages 6 hours after re-stimulation. n = 3. (E-F), Percent of VSV-GFP-infected control– or polyIC-stimulated control– or polyIC-experienced in vitro cultured alveolar macrophages after 5 (E) and 14 days (F). n = 4. Data are mean ± s.e.m. n values indicate the number of mice or replicates. For (A-F), statistics were calculated using Student's t-test with Bonferroni correction when multiple comparisons were performed. *p < 0.05; **p < 0.01; ***p < 0.001.

Figure 5

Figure 5: Past SARS-CoV-2 infection ameliorates secondary influenza A virus infection.
(A) Body weights of naïve and SARS-CoV-2-recovered animals infected with influenza A/PR/8/34 virus at LD50 (naïve/PR8 or SARS2/PR8). n = 5. (B) Survival percentages of naïve/PR8 and SARS2/PR8 animals. n = 5. (C-F) Kinetics of neutrophils (C), alveolar macrophages (D), NK cells (E) and CD8 T cells (F) in bronchoalveolar lavage fluid (BALF) of naïve/PR8 and SARS2/PR8 animals. n = 3-7. (G) Significantly different cytokines and chemokines in BALF of naïve/PR8 and SARS2/PR8 animals at 5 days after PR8 infection. n = 4-5. (H) UMAP clustering and major cell cluster annotation of single cell RNA-seq data of BALF from naïve/PR8 and SARS2/PR8 animals at 7 days post PR8 infection. (I) Gene ontology (GO) enrichment analyses of genes associated with cells isolated from naïve/PR8 or SARS2/PR8 BALF in macrophages cluster 1 (G). Data are mean ± s.e.m. n values indicate the number of mice or replicates. For (A), statistical analysis was performed using Two-Way ANOVA comparison with Bonferroni correction. For (B), statistical analysis was performed using a log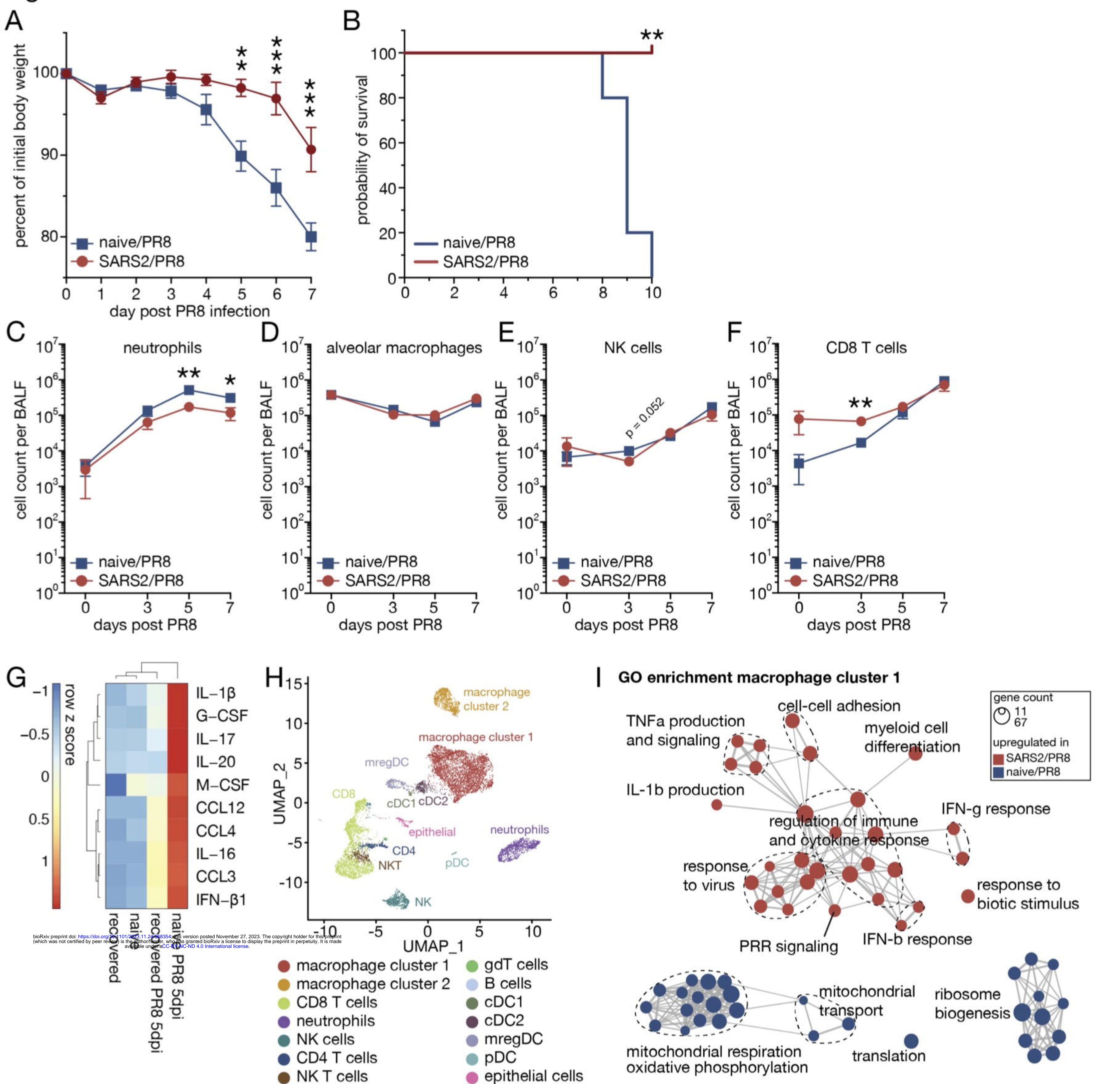-rank Mantel-Cox test. For (C-G), statistics were calculated using Student's t-test with Bonferroni correction when multiple comparisons were performed. For (I), hypergeometric p values were adjusted for multiple testing with Benjamini-Hochberg correction. *p < 0.05; **p < 0.01; ***p < 0.001.

Figure S5

Figure S5: Characterization of pathology of naïve and SARS-CoV-2-recovered animals superinfected with influenza A/PR/8/34 virus
(A) Body weights of naïve and SARS-CoV-2-recovered animals infected with a sub-lethal dose of influenza A/PR/8/34 virus (naïve/PR8 or SARS2/PR8). n = 5-6. (B) RT-qPCR analyses of influenza A virus matrix protein (M1) transcript levels in naïve/PR8 or SARS2/PR8 animals. n = 5-7. (C) Gene ontology (GO) enrichment analyses of differentially expressed genes (DEG) of macrophage cluster 1 vs. macrophage cluster 2 identified in single cell RNA-sequencing (scRNA-seq) of bronchoalveolar lavage fluid (BALF) in naïve/PR8 or SARS2/PR8 animals at 7 days post PR8 infection. (D) Split violin plot of ISG gene set expression between any major cell populations and conditions identified by scRNA-seq (C). (E) GO enrichment analyses of DEG of neutrophils isolated from naïve/PR8 or SARS2/PR8 animals. Data are mean ± s.e.m. n values indicate the number of mice or replicates. (F) GO enrichment analyses of DEG of CD8 T cells isolated from naïve/PR8 or SARS2/PR8 animals. Data are mean ± s.e.m. n values indicate the number of mice or replicates. For (A), statistical analysis was performed using Two-Way ANOVA comparison with Bonferroni correction. For (B), statistics were calculated using Student's t-test with Bonferroni correction when multiple comparisons were performed. For (C-F), DEG were identified using Wilcoxon rank sum test with Bonferroni correction. For (C-E and F), hypergeometric p values were adjusted for multiple testing with Benjamini-Hochberg correction. *p < 0.05; **p < 0.01; ***p < 0.001.